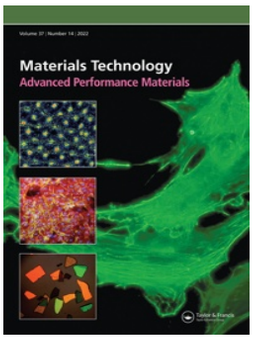

Taylor & Francis
Taylor & Francis Group

Materials Technology
Advanced Performance Materials

ISSN: 1066-7857 (Print) 1753-5557 (Online) Journal homepage: www.tandfonline.com/journals/ymte20

Machine-learning-assisted multilayer graphene–silver–ZrN surface plasmon resonance biosensor for high-sensitivity hemoglobin detection

William Ochen, Jacob Wekalao, Jonas Muheki, Hussein A. Elsayed, Haifa A. Alqhtani, Abdulkarem H. M. Almawgani, Adam R. Alhawari, Ahmed Mehaney & Emad Solouma

To cite this article: William Ochen, Jacob Wekalao, Jonas Muheki, Hussein A. Elsayed, Haifa A. Alqhtani, Abdulkarem H. M. Almawgani, Adam R. Alhawari, Ahmed Mehaney & Emad Solouma (2026) Machine-learning-assisted multilayer graphene–silver–ZrN surface plasmon resonance biosensor for high-sensitivity hemoglobin detection, Materials Technology, 41:1, 2621020, DOI: 10.1080/10667857.2026.2621020

To link to this article: https://doi.org/10.1080/10667857.2026.2621020

Published online: 09 Feb 2026.

MATERIALS TECHNOLOGY
2026, VOL. 41, NO. 1, 2621020
https://doi.org/10.1080/10667857.2026.2621020

Taylor & Francis
Taylor & Francis Group

RESEARCH ARTICLE

OPEN ACCESS Check for updates

Machine-learning-assisted multilayer graphene–silver–ZrN surface plasmon resonance biosensor for high-sensitivity hemoglobin detection

William Ochen[a], Jacob Wekalao[b], Jonas Muheki[a], Hussein A. Elsayed[c], Haifa A. Alqhtani[d], Abdulkarem H. M. Almawgani[e], Adam R. Alhawari[f], Ahmed Mehaney[e] and Emad Solouma[g]

[a]Department of Physics, Kyambogo University, Kampala, Uganda; [b]Department of Optics and Optical Engineering, University of Science and Technology of China, Hefei, People's Republic of China; [c]Department of Physics, College of Science, University of Ha'il, Ha'il, Saudi Arabia; [d]Department of Biology, College of Science, Princess Nourah bint Abdulrahman University, Riyadh, Saudi Arabia; [e]Department of Electrical Engineering, College of Engineering, Najran University, Najran, Saudi Arabia; [f]Physics Department, Faculty of Science, Beni-Suef University, Beni Suef, Egypt; [g]Department of Mathematics and Statistics, College of Science, Imam Mohammad Ibn Saud Islamic University (IMSIU), Riyadh, Saudi Arabia

ABSTRACT

This work presents a theoretically optimized multilayer surface plasmon resonance (SPR) biosensor for quantitative hemoglobin detection using the Kretschmann configuration. The sensor integrates a BK-7 prism, silver plasmonic layer, graphene enhancement layer, zirconium nitride (ZrN) protective layer, and aqueous sensing medium. This architecture synergistically combines enhanced electromagnetic confinement with chemical stability, addressing silver's oxidation vulnerability while maintaining superior plasmonic performance. Electromagnetic analysis via transfer matrix method and finite-element simulations demonstrates exceptional sensitivity metrics: maximum angular sensitivity of 500°/RIU, figure of merit of 92.25 RIU^{-1}, and detection limit of 0.006 RIU across clinically relevant hemoglobin concentrations (10–40 g/L). Localized electric field enhancement (~10^6 V/m) at the sensing interface confirms optimal light-matter interaction amplification. Machine learning models predict sensor responses to graphene thickness and refractive index variations with $R^2 > 0.99$, enabling rapid optimization. This design advances SPR biosensor technology for sensitive, label-free biochemical detection applications.

ARTICLE HISTORY
Received 5 November 2025
Accepted 17 January 2026

KEYWORDS
Surface plasmon resonance; hemoglobin detection; graphene-based biosensor; machine learning optimization; multilayer plasmonics; electromagnetic field enhancement; fresnel boundary conditions

Introduction

Since their first demonstration in the 1980s, surface plasmon resonance (SPR) biosensors have evolved into indispensable analytical instruments, primarily valued for their ability to perform label-free, real-time monitoring of biomolecular interactions [1,2]. The underlying physics of SPR involves the interaction of photons with free electrons at a metal-dielectric interface, which triggers collective oscillations known as surface plasmon polaritons [3]. These oscillations generate evanescent waves that are exceptionally sensitive to changes in the refractive index within a 200–300 nm proximity of the metal surface [4–8]. This sensitivity makes SPR an ideal mechanism for detecting the minute shifts caused by biomolecular binding events [9]. Among various experimental setups, the Kretschmann configuration remains the industry standard. Its enduring popularity stems from its practical advantages, including high coupling efficiency, ease of implementation, and versatility across different optical interrogation modes such as angular, wavelength, and intensity modulation [10,11].

The choice of plasmonic material is perhaps the most critical factor in determining a sensor's performance [12–16]. While gold is the traditional choice due to its chemical stability, silver offers superior plasmonic characteristics, including sharper resonance dips and higher sensitivity resulting from lower damping losses [17,18]. Research by Sharma and Gupta [19] highlighted that silver-based

CONTACT William Ochen wocen@kyu.ac.ug Department of Physics, Kyambogo University, Kampala, Uganda; Jacob Wekalao jacob1902@mail.ustc.edu.cn Department of Optics and Optical Engineering, University of Science and Technology of China, Hefei, 230026, People's Republic of China

SPR sensors could achieve detection limits in the nanomolar range [20–22]. However, silver is highly susceptible to oxidation and remains chemically unstable in biological environments. This vulnerability has limited its widespread adoption, creating an urgent need for protective overlayers that can shield the metal without compromising its plasmonic advantages [23–26].

Over the last two decades, the integration of nanomaterials has revolutionised the capabilities of SPR sensors. Jay et al. reported a femtosecond-laser-fabricated dual-channel H-shaped fibre SPR sensor enabling simultaneous refractive index (1.30–1.39) and temperature (20–60°C) detection with ultra-high sensitivities of 8,400 nm/RIU and 37.6 nm/°C [27]. Butt et al. reviewed SPR-based biodetection systems, outlining their fundamental operating principles, recent technological advancements in materials and nanostructures [28]. Kokhli et al. presented a comprehensive review of fibre-optic LSPR-based plasmonic sensors, highlighting their high sensitivity and selectivity, integration advantages, and advanced applications in biological, chemical, and physical sensing for real-time and precise detection [29]. Kushwaha et al. theoretically proposed and optimised a fibre-optic SPR sensor incorporating $BaTiO_3$ and Si layers for dual monitoring of aqueous (RI 1.33–1.37) and gaseous (down to RI 1.01) impurities, achieving ultrahigh sensitivity, linear NIR response, and single-probe environmental sensing capability [30]. Ma et al. demonstrated that a composite Ag NPs–PSi Bragg reflector SERS substrate enables noninvasive early breast cancer serum detection with high diagnostic accuracy (95%), specificity (96.7%), and sensitivity (93.3%) [31]. Li et al. developed a preamplification-free nanozyme-based TSA strategy that enables sensitive and specific colorimetric detection of low-abundance miRNA in biological samples, facilitating acute myocarditis diagnosis [32]. He et al. developed a nanographite-based fluorescent biosensor with DSN-assisted signal amplification that enables highly sensitive and selective detection of miRNA down to 10 pmol/L, with potential applications in disease diagnosis and biochemical research [33]. Tang et al. reviewed recent advances in bacterial aptamer-based sensors, highlighting their high affinity, selectivity, and stability, and discussed optical and electrochemical detection strategies, technological innovations, and future prospects for rapid bacterial diagnostics [34]. Yi et al. summarised the development of aptamer-based biosensors for rapid detection of microorganisms, including bacteria, viruses, and toxins, covering optical, electrochemical, and hybrid sensing technologies for public health applications [35]. Li et al. developed a nanozyme-based colorimetric sensor array combined with deep learning (YOLOv8) for intelligent, highly sensitive, and automatic detection of multiple pesticide residues, achieving a detection limit below 0.0012 μM with rapid and accurate classification [36]. Du et al. developed an ultrasensitive twisted bilayer graphene–Au nanodisk CRISPR-Cas12a biosensor enabling label-free, real-time nucleic acid detection down to 44.63 aM, combining moiré-engineered optoelectronics with programmable bio-nanoarrays for precision diagnostics [37]. Chen et al. developed MOPCS, a CRISPR-Cas12a–empowered SPR platform enabling rapid, amplification-free detection of SARS-CoV-2 and its variants with high sensitivity (15 fM) and specificity within 38 minutes [38]. Chen et al. reported a low-cost CRISPR/Cas12a-empowered SPR platform (MOPCS) that enables rapid, amplification-free, and highly sensitive (15 fM) detection and discrimination of SARS-CoV-2 variants, including Delta and Omicron, within 38 min [39]. Du et al. demonstrated an ultrasensitive tBLG–Au nanodisk–CRISPR/Cas12a optoelectronic biosensor achieving sub-femtomolar (44.63 aM) amplification-free miRNA detection via VHS–plasmon resonance coupling and dielectric modulation, validated on lung cancer samples with qPCR-level accuracy [40]. Li et al. developed a low-cost Cu–amino-acid nanozyme colorimetric sensor array integrated with YOLOv8 deep learning, enabling highly accurate (mAP = 0.99) and ultrasensitive (<0.0012 μM) intelligent detection of multiple pesticide residues [41]. He et al. proposed a high-accuracy spherical wavefront calibration for Shack–Hartmann wavefront sensors using a 1 μm pinhole, achieving λ/1000 RMS accuracy after residual error correction and demonstrating stable, precise wavefront measurements for advanced optical systems [42]. Singh et al. proposed a Kretschmann-configured SPR sensor using Ag/Pt/antimonene/chitosan that enables highly sensitive and selective formalin detection, achieving a maximum sensitivity of 206.86°/RIU with strong interfacial field enhancement [43]. Kumar et al. reported a Ga-doped ZnO/MXene-based SPR sensor achieving enhanced sensitivity of 264.59°/RIU with high detection accuracy and FOM, demonstrating its suitability for sensitive biomolecular and biochemical detection [44]. Tiwari et al. demonstrated a deep learning–assisted Au-TFBG sensing framework using a hierarchical composite attention LSTM to enhance spectral data quality, achieving highly accurate transmittance prediction and improved sensor performance evaluation [45]. Rana et al. applied explainable machine learning to an SPR-based fibre-optic

sensor, showing that CatBoost with SHAP analysis accurately predicts and interprets the figure of merit, with analyte refractive index and wavelength as dominant performance drivers [46]. Srivastava et al. employed an inverse-design SPR optimisation using PSO–TMM to overcome sensitivity–accuracy trade-offs, achieving an ultra-high sensitivity of 630.54°/RIU and FoM of 2277 RIU^{-1}, outperforming existing SPR sensor designs [47]. Tiwari et al. proposed a DL-assisted Seq2Seq-attention RNN framework for rapid extrapolation of fibre-optic sensor performance, achieving accurate FOM prediction with sub-second computation and over 100 × speedup compared to conventional simulations [48]. Rastogi et al. demonstrated a hybrid ML–PSO approach for rapid SPR sensor design, achieving a sensitivity of 68.754°/RIU and FoM of 100, with optimisation speeds four orders of magnitude faster than conventional electromagnetic calculations.

Despite these advancements, the application of SPR to haemoglobin (Hb) detection remains relatively underexplored. This is a significant omission, given that haemoglobin is a critical clinical biomarker for conditions like anaemia, which affects roughly 1.62 billion people worldwide [49–53]. While some progress has been made. Building on the foundations of nanomaterial-enhanced SPR and addressing the clinical demand for better haemoglobin diagnostics, this work proposes a simple multilayer biosensor architecture. Designed for high sensitivity and selectivity, the sensor utilises a Kretschmann configuration consisting of a BK-7 prism/graphene/silver/carbon nanotube/biosample stack. This design synergistically pairs the superior plasmonic properties of silver with the protective stability of graphene and the amplification power of carbon nanotubes. It should be emphasised that the present work constitutes a theoretical and numerical investigation intended to establish an optimised design framework for haemoglobin-sensitive SPR biosensors. While experimental validation is beyond the scope of this study, all materials, layer thicknesses, and optical configurations employed herein are compatible with standard nanofabrication and SPR characterisation techniques. The primary contribution of this work lies in the optimised multilayer SPR sensor design that achieves high sensitivity and sharp resonance characteristics for haemoglobin detection. Machine learning is incorporated as a complementary computational framework that enables rapid prediction and optimisation of sensor response across multidimensional parameter spaces, rather than as a replacement for physics-based electromagnetic modelling.

Design consideration and refractive index

Figure 1 displays the proposed multi-layered SPR biosensor architecture designed for haemoglobin concentration detection. The foundation of this sensor is a BK-7 prism that serves as the optical coupling device with a refractive index of 1.5151 at the operating wavelength. This prism enables the excitation of surface plasmon waves through the Kretschmann configuration, allowing incident light to interact with the metallic layer at specific angles to achieve resonance conditions. Adjacent to the prism is the silver layer, which functions as the primary plasmonic material with an optimised thickness range of 25–49 nm and a complex refractive index of 0.0803 + 4.2347i. This layer generates surface plasmon polaritons at the metal-dielectric interface. Silver is specifically chosen for its superior plasmonic properties, including low optical losses and sharp resonance characteristics in the visible spectrum, which contribute to enhanced sensor performance and precise detection capabilities. The third layer consists of graphene with an optimised thickness of 0.2–1.4 nm, corresponding to approximately 1–4 monolayers, and a refractive index of 2.7411 + 1.4017i. This layer serves dual purposes as both a biomolecular adsorption platform and a sensitivity enhancer. Graphene's atomically thin two-dimensional structure, exceptional electrical conductivity, high surface-to-volume ratio, and biocompatibility make it particularly suitable for improving biosensor sensitivity. The layer facilitates stronger biomolecular interactions and increases the evanescent field intensity, thereby amplifying the refractive index changes induced by analyte binding and ultimately improving the sensor's detection limits. Following the graphene layer is a zirconium nitride layer with an optimised thickness range of 2–14 nm and a refractive index of 0.63 + 2.75292i. This transition metal nitride acts as an additional plasmonic and protective component that exhibits excellent chemical stability, biocompatibility, and tunable optical properties. The ZrN layer further enhances the electric field distribution at the sensor surface, improves adhesion between adjacent layers, and provides protection against oxidation while maintaining the sensor's plasmonic response. These characteristics contribute to both the sensitivity and longevity of the biosensor device. The outermost layer serves as the sensing

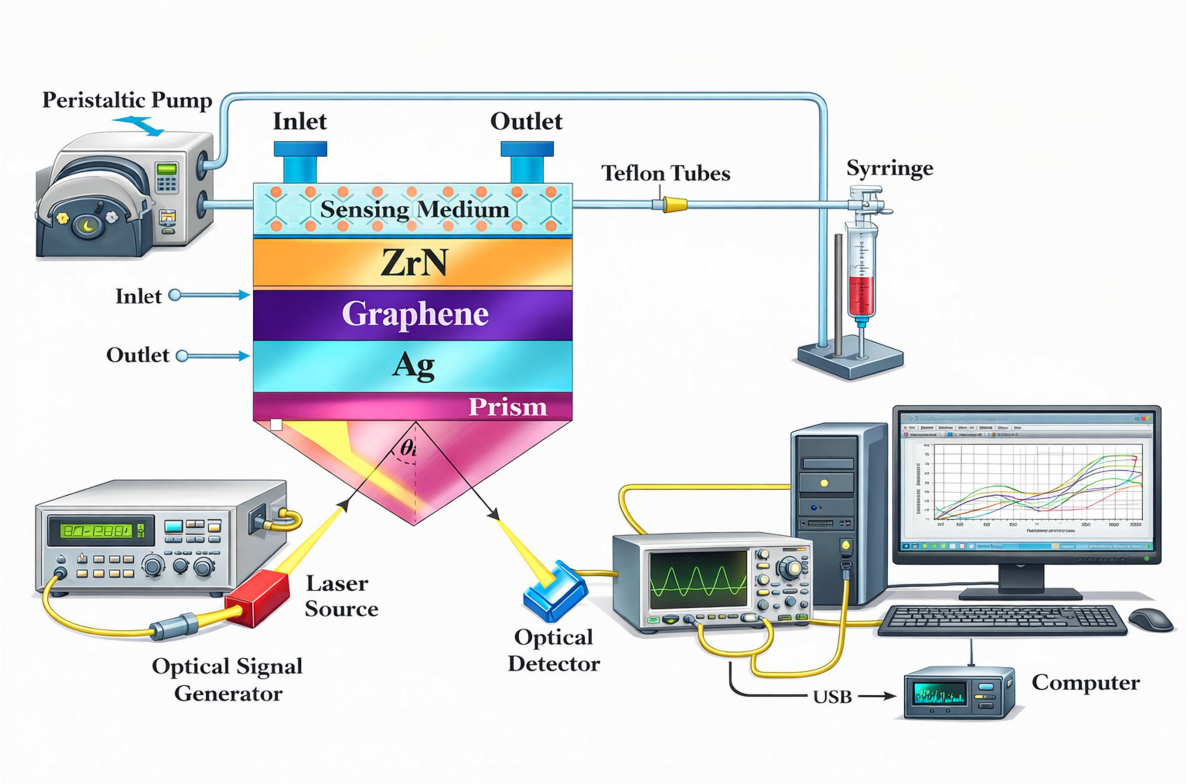

Figure 1. Schematic diagram of the five-layer SPR biosensor configuration consisting of BK-7 prism, silver (Ag) plasmonic layer, graphene sensitivity enhancement layer, zirconium nitride (ZrN) optimisation layer, and sensing medium for haemoglobin concentration detection.

medium for haemoglobin concentration detection. This aqueous analyte layer has variable refractive index values that depend on the haemoglobin concentration present in the sample. Changes in haemoglobin levels alter the refractive index of this medium, which subsequently shifts the SPR resonance angle or wavelength. This shift enables quantitative detection and measurement of haemoglobin concentrations in biological samples such as whole blood or haemolyzed solutions, making the biosensor suitable for clinical diagnostic applications and haematological analysis.

The fabrication of the proposed plasmonic sensor follows standard micro- and nano-fabrication practices commonly employed in optical and plasmonic engineering laboratories. Initially, a high-refractive-index prism substrate is thoroughly cleaned using sequential solvent and plasma treatments to eliminate organic and particulate contaminants. A thin silver (Ag) film is then deposited onto the prism surface using physical vapour deposition techniques such as electron-beam evaporation or magnetron sputtering, ensuring uniform thickness and low surface roughness to support stable surface plasmon resonance excitation. Subsequently, a monolayer or few-layer graphene sheet, typically synthesised via chemical vapour deposition (CVD), is transferred onto the Ag layer using a polymer-assisted wet transfer method. This graphene layer enhances charge carrier mobility and improves plasmon confinement at the metal–dielectric interface. Following graphene integration, a zirconium nitride (ZrN) layer is deposited using reactive sputtering, providing high thermal stability, strong plasmonic response, and improved chemical robustness compared to noble metals alone. The completed multilayer stack is then patterned or encapsulated with a microfluidic sensing chamber, incorporating precisely aligned inlet and outlet ports for controlled analyte delivery. Final assembly includes optical alignment of the laser source and detector at the prism interface, electrical and optical interfacing with signal generators and data acquisition systems, and real-time monitoring through a computer-based analysis platform. This end-to-end fabrication and integration process results in a robust, experimentally realisable plasmonic sensor suitable for high-impact (Q1) scientific investigations and practical biosensing applications (Figure 2).

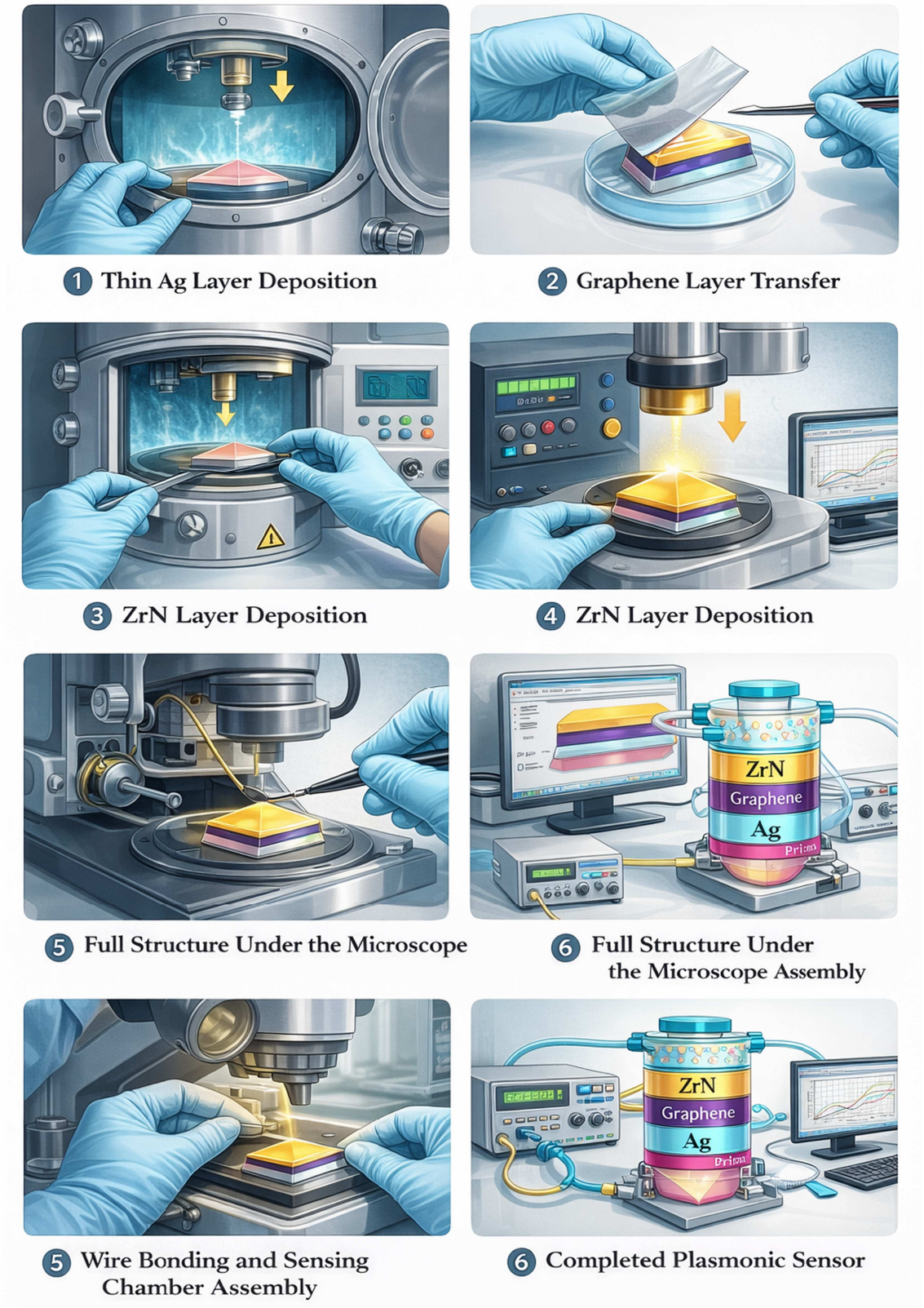

Figure 2. Schematic illustration of the complete plasmonic biosensor system and its fabrication workflow. The figure presents (i) the multilayer SPR sensor architecture consisting of a prism/Ag/graphene/ZrN stack integrated with a microfluidic sensing chamber, (ii) the optical interrogation setup including a laser source, optical signal generator,

(*Caption on next page*)

prism coupler, and photodetector, all interfaced with a computer-based data acquisition and analysis unit, and (iii) representative fabrication stages employed by engineers, such as thin-film deposition, graphene transfer, layer integration, and final device assembly for experimental characterisation.

Electromagnetic analysis of multi-layered SPR biosensor for haemoglobin detection

Time-harmonic Maxwell equations in stratified media

The electromagnetic wave propagation through the multi-layered plasmonic biosensor is governed by Maxwell's equations in their time-harmonic form, which constitute the fundamental framework for analysing light-matter interactions at the nanoscale metal-dielectric interfaces.

$$\nabla \times \mathbb{E}(\mathbf{r}, \omega) = i\omega\mu_0 \mathbb{H}(\mathbf{r}, \omega)$$

$$\nabla \times \mathbb{H}(\mathbf{r}, \omega) = -i\omega\varepsilon_0 \tilde{\varepsilon}(\mathbf{r}, \omega)\mathbb{E}(\mathbf{r}, \omega)$$

$$\nabla \cdot [\tilde{\varepsilon}(\mathbf{r}, \omega)\mathbb{E}(\mathbf{r}, \omega)] = 0$$

$$\nabla \cdot \mathbb{H}(\mathbf{r}, \omega) = 0$$

where $\mathbb{E}(\mathbf{r}, \omega)$ and $\mathbb{H}(\mathbf{r}, \omega)$ represent the complex electric and magnetic field phasors respectively, $\omega = 2\pi c/\lambda$ denotes the angular frequency, $\mu_0 = 4\pi \times 10^{-7}$ H/m is the vacuum permeability, $\varepsilon_0 = 8.854 \times 10^{-12}$ F/m is the vacuum permittivity, and $\tilde{\varepsilon}(\mathbf{r}, \omega) = \varepsilon'(\omega) + i\varepsilon''(\omega)$ represents the position-dependent complex relative permittivity tensor that characterises the optical response of each constituent layer.

Transfer matrix formalism for stratified anisotropic systems

The optical response of the N-layer heterostructure is analytically described through the transfer matrix method, which provides a systematic approach to solve boundary value problems in stratified media by connecting electromagnetic field amplitudes across successive interfaces through characteristic propagation matrices.

$$\mathcal{R}_p(\theta, \omega) = \left| \frac{(\mathbb{M}_{11} + \mathbb{M}_{12}\varsigma_N)\varsigma_0 - (\mathbb{M}_{21} + \mathbb{M}_{22}\varsigma_N)}{(\mathbb{M}_{11} + \mathbb{M}_{12}\varsigma_N)\varsigma_0 + (\mathbb{M}_{21} + \mathbb{M}_{22}\varsigma_N)} \right|^2$$

$$\mathbb{M} = \prod_{j=1}^{N-1} \mathbb{L}_j = \mathbb{L}_1 \otimes \mathbb{L}_2 \otimes \mathbb{L}_3 \otimes \cdots \otimes \mathbb{L}_{N-1}$$

$$\mathbb{L}_j = \begin{bmatrix} \cos(\Phi_j) & -i\varsigma_j^{-1} \sin(\Phi_j) \\ -i\varsigma_j \sin(\Phi_j) & \cos(\Phi_j) \end{bmatrix}$$

$$\Phi_j = \frac{2\pi h_j}{\lambda_0} \sqrt{\tilde{n}_j^2 - n_0^2 \sin^2\theta} = k_0 h_j \kappa_{z,j}$$

$$\varsigma_j = \frac{\sqrt{\tilde{n}_j^2 - n_0^2 \sin^2\theta}}{\tilde{n}_j^2} = \frac{\kappa_{z,j}}{\tilde{n}_j^2 k_0}$$

where $\mathcal{R}_p(\theta, \omega)$ is the p-polarised reflectance, $\mathbb{M}$ represents the cumulative system matrix with elements $\mathbb{M}_{mn}$, $\mathbb{L}_j$ denotes the characteristic matrix for layer j, $\otimes$ symbolises matrix multiplication, Φ_j is the complex phase thickness, h_j is the physical thickness of layer j, λ_0 is the vacuum wavelength, $\tilde{n}_j = n_j' + in_j''$ is the

complex refractive index, $k_0 = 2\pi/\lambda_0$ is the free-space wavevector magnitude, $\kappa_{z,j}$ is the normalised z-component of the wavevector, ς_j represents the generalised optical admittance for p-polarisation, and θ is the incident angle measured from the surface normal.

Surface plasmon polariton dispersion relation

The surface plasmon resonance condition manifests when the tangential wavevector component of the incident photon equals the real part of the surface plasmon polariton propagation constant, enabling coherent momentum matching and collective electron oscillation at the metal-dielectric interface.

$$\mathfrak{k}_{\parallel}^{(SPP)}(\omega) = \frac{\omega}{c}\sqrt{\frac{\tilde{\varepsilon}_m(\omega)\cdot\tilde{\varepsilon}_{d,eff}(\omega)}{\tilde{\varepsilon}_m(\omega)+\tilde{\varepsilon}_{d,eff}(\omega)}} = k_0\sqrt{\frac{\tilde{\varepsilon}_m\tilde{\varepsilon}_{d,eff}}{\tilde{\varepsilon}_m+\tilde{\varepsilon}_{d,eff}}}$$

$$k_0 n_0 \sin\theta_{res} = \Re[\mathfrak{k}_{\parallel}^{(SPP)}]$$

$$\sin\theta_{res} = \frac{1}{n_0}\Re\left[\sqrt{\frac{\tilde{\varepsilon}_m(\omega)\tilde{\varepsilon}_{d,eff}(\omega)}{\tilde{\varepsilon}_m(\omega)+\tilde{\varepsilon}_{d,eff}(\omega)}}\right]$$

$$\tilde{\varepsilon}_{d,eff} = \mathcal{F}[\tilde{\varepsilon}_{Gr}(h_2,\mu_c),\tilde{\varepsilon}_{ZrN}(h_3),\tilde{\varepsilon}_{analyte}(\mathcal{C}_{Hb})]$$

$$\mathscr{L}_{prop}^{(SPP)} = \frac{1}{2\Im[\mathfrak{k}_{\parallel}^{(SPP)}]} = \frac{\lambda_0}{4\pi}\left(\frac{\tilde{\varepsilon}_m+\tilde{\varepsilon}_d}{\tilde{\varepsilon}_m\tilde{\varepsilon}_d}\right)^{3/2}\left(\frac{\varepsilon_m'}{\varepsilon_m''}\right)^2$$

where $\mathfrak{k}_{\parallel}^{(SPP)}$ is the complex surface plasmon polariton wavevector, c is the speed of light, $\tilde{\varepsilon}_m$ denotes the frequency-dependent complex permittivity of the metallic (silver) layer, $\tilde{\varepsilon}_{d,eff}$ represents the effective permittivity of the composite dielectric environment, θ_{res} is the resonance angle, $\Re[\cdot]$ and $\Im[\cdot]$ denote real and imaginary parts respectively, $\mathcal{F}$ is a functional operator describing the effective medium approximation, $\tilde{\varepsilon}_{Gr}$ is the graphene permittivity dependent on thickness h_2 and chemical potential μ_c, $\tilde{\varepsilon}_{ZrN}$ is the zirconium nitride permittivity, $\mathcal{C}_{Hb}$ represents haemoglobin concentration, and $\mathcal{L}_{prop}^{(SPP)}$ denotes the surface plasmon propagation length.

Electromagnetic field enhancement and spatial distribution

The electric field intensity distribution across the heterostructure exhibits pronounced amplification at the plasmonic interface, with evanescent wave characteristics in the sensing region determining the effective probe volume for biomolecular interactions.

$$\mathbb{E}_j(\zeta) = \mathbb{E}_0\cdot\mathscr{T}_j(\theta)[\exp(i\kappa_{z,j}\zeta)+\mathcal{R}_j^{(\mathrm{int})}\exp(-i\kappa_{z,j}\zeta)] \tag{1}$$

$$\mathcal{J}_j(\zeta) = \frac{|\mathbb{E}_j(\zeta)|^2}{|\mathbb{E}_0|^2} = \left|\frac{2\varsigma_0}{(\mathbb{M}_{11}+\mathbb{M}_{12}\varsigma_N)\varsigma_0+(\mathbb{M}_{21}+\mathbb{M}_{22}\varsigma_N)}\right|^2|\exp(i\kappa_{z,j}\zeta)+\mathcal{R}_j^{(\mathrm{int})}\exp(-i\kappa_{z,j}\zeta)|^2$$

$$\Xi_{enhancement} = \frac{|\mathbb{E}_{interface}|^2}{|\mathbb{E}_0|^2}\Big|_{\theta=\theta_{res}} = \frac{4|\varsigma_0|^2}{|(\mathbb{M}_{11}+\mathbb{M}_{12}\varsigma_N)\varsigma_0+(\mathbb{M}_{21}+\mathbb{M}_{22}\varsigma_N)|^2}\Big|_{\theta_{res}} \tag{2}$$

$$\delta_{pen}(\omega,\theta_{res}) = \frac{1}{2|\Im[\kappa_{z,N}]|} = \frac{\lambda_0}{4\pi|\Im[\sqrt{\tilde{n}_N^2-n_0^2\sin^2\theta_{res}}]|} \tag{3}$$

$$\mathcal{J}(\zeta > 0) = \mathcal{J}_0 \exp\left(0|\frac{2\zeta}{\delta_{pen}}\right) \text{for } \zeta \text{ in sensing medium} \tag{4}$$

where $\mathbb{E}_j(\zeta)$ is the electric field phasor at position ζ within layer j, $\mathcal{T}_j$ is the cumulative transmission amplitude, $\mathcal{R}_j^{(\text{int})}$ represents internal reflection coefficients, $\mathcal{J}_j$ denotes normalised intensity, $\Xi_{enhancement}$ quantifies the field enhancement factor, δ_{pen} is the penetration depth of the evanescent wave into the sensing medium, and $\mathcal{J}_0$ is the surface intensity at the interface.

Graphene optical conductivity and dielectric response

The atomically thin graphene layer exhibits unique optoelectronic properties described by the Kubo formalism, where both intraband (Drude) and interband transitions contribute to its frequency-dependent complex conductivity, thereby modulating the plasmonic field distribution.

$$\tilde{\sigma}_{Gr}(\omega, \mu_c, T, \tau) = \sigma_{intra}(\omega, \mu_c, T, \tau) + \sigma_{inter}(\omega, \mu_c, T) \tag{5}$$

$$\sigma_{intra}(\omega) = \frac{ie^2 k_B T}{\pi\hbar^2(\omega + i\tau^{-1})}\left[\frac{\mu_c}{k_B T} + 2\ln\left(\exp\left(0|\frac{\mu_c}{k_B T}\right) + 1\right)\right] \tag{6}$$

$$\sigma_{inter}(\omega) = \frac{e^2}{4\hbar}\left[\mathcal{G}\left(\frac{\hbar\omega}{2}\right)|i\frac{4\hbar\omega}{\pi}\int_0^\infty \frac{\mathcal{G}(\xi) - \mathcal{G}(\hbar\omega/2)}{(\hbar\omega)^2|4\xi^2)}d\xi\right] \tag{7}$$

$$\mathcal{G}(\xi) = \frac{\sinh\ (\xi/k_B T)}{\cosh\ (\mu_c/k_B T) + \cosh\ (\xi/k_B T)} \tag{8}$$

$$\tilde{\varepsilon}_{Gr}(\omega) = \varepsilon_\infty + i\frac{\tilde{\sigma}_{Gr}(\omega)}{\omega\varepsilon_0 h_{Gr}} \tag{9}$$

where $\tilde{\sigma}_{Gr}$ is the complex surface conductivity of graphene, μ_c is the chemical potential (Fermi level), T is absolute temperature, τ is the momentum relaxation time, e is the elementary charge, $\hbar$ is the reduced Planck constant, k_B is Boltzmann's constant, $\mathcal{G}(\xi)$ is the distribution function, ε_∞ is the high-frequency permittivity, and $h_{Gr} = N_{layer} \times 0.335$ nm represents the effective graphene thickness with N_{layer} monolayers.

Sensitivity tensor and detection metrics

The sensor's analytical performance is quantified through sensitivity metrics that relate the resonance parameter shifts to refractive index perturbations in the sensing layer, with the figure of merit providing a comprehensive assessment of detection capability.

$$\mathfrak{S}_\theta = \frac{\partial\theta_{res}}{\partial n_N}|_{n_N = n_N^{(0)}} = -\frac{2\tan\theta_{res}}{n_0}\cdot\frac{\partial}{\partial n_N}\left[\Re\sqrt{\frac{\tilde{\varepsilon}_m\tilde{\varepsilon}_{d,eff}}{\tilde{\varepsilon}_m + \tilde{\varepsilon}_{d,eff}}}\right] \tag{10}$$

$$\mathfrak{S}_\lambda = \frac{\partial\lambda_{res}}{\partial n_N}|_{n_N = n_N^{(0)}}; \mathfrak{S}_C = \mathfrak{S}_\theta\cdot\frac{\partial n_N}{\partial\mathscr{C}_{Hb}} = \mathfrak{S}_\theta\cdot\alpha_{Hb} \tag{11}$$

$$\Omega_{FWHM} = \theta_+ - \theta_- where\mathcal{R}_p(\theta_\pm) = \frac{\mathcal{R}_{\max} + \mathcal{R}_{\min}}{2} \tag{12}$$

$$\mathcal{Q}_{FOM} = \frac{\mathfrak{S}_\theta}{\Omega_{FWHM}} = \frac{|\partial\theta_{res}/\partial n_N|}{\Omega_{FWHM}} \tag{13}$$

$$\Delta n_{LOD} = \frac{\Omega_{FWHM} \cdot \sigma_\theta^{(noise)}}{\mathfrak{S}_\theta}; \Delta \mathcal{C}_{LOD} = \frac{\Delta n_{LOD}}{\alpha_{Hb}} \tag{14}$$

where $\mathfrak{S}_\theta$ is the angular sensitivity (deg/RIU), $\mathfrak{S}_\lambda$ is the wavelength sensitivity (nm/RIU), $\mathfrak{S}_\mathcal{C}$ represents concentration sensitivity (deg·dL/g), $\alpha_{Hb} \approx 1.9 \times 10^{-3}$ dL/g is the specific refractive index increment for haemoglobin, Ω_{FWHM} denotes the full-width at half-maximum of the resonance dip, $\mathcal{Q}_{FOM}$ is the figure of merit (RIU^{-1}), Δn_{LOD} is the limit of detection for refractive index, $\sigma_\theta^{(noise)}$ represents angular measurement noise, and $\Delta \mathcal{C}_{LOD}$ is the minimum detectable haemoglobin concentration.

Multi-objective optimisation framework

The optimal geometric configuration of the multi-layered architecture is determined through a constrained variational approach that simultaneously minimises reflectance at resonance while maximising sensitivity and figure of merit within physically realisable parameter spaces.

$$\min_{\{h_1|h_2|h_3\}} \Psi(h_1, h_2, h_3) = \min_{\{h_1|h_2|h_3\}} [\omega_1 \mathcal{R}_{\min} | \omega_2 \mathfrak{S}_\theta | \omega_3 \mathcal{Q}_{FOM}] \tag{15}$$

$$\text{subject to:} \begin{cases} h_1^{(\min)} \le h_1 \le h_1^{(\max)} & \text{(Silver: 25–49 nm)} \\ h_2^{(\min)} \le h_2 \le h_2^{(\max)} & \text{(Graphene: 0.2–1.4 nm)} \\ h_3^{(\min)} \le h_3 \le h_3^{(\max)} & \text{(ZrN: 2–14 nm)} \end{cases} \tag{16}$$

$$\nabla_{h_j} \Psi |_{h_j = h_j^{(opt)}} = 0 \; for \; j \in \{1, 2, 3\} \tag{17}$$

$$\mathcal{H}(\Psi) = \begin{bmatrix} \frac{\partial^2 \Psi}{\partial h_1^2} & \frac{\partial^2 \Psi}{\partial h_1 \partial h_2} & \frac{\partial^2 \Psi}{\partial h_1 \partial h_3} \\ \frac{\partial^2 \Psi}{\partial h_2 \partial h_1} & \frac{\partial^2 \Psi}{\partial h_2^2} & \frac{\partial^2 \Psi}{\partial h_2 \partial h_3} \\ \frac{\partial^2 \Psi}{\partial h_3 \partial h_1} & \frac{\partial^2 \Psi}{\partial h_3 \partial h_2} & \frac{\partial^2 \Psi}{\partial h_3^2} \end{bmatrix} \succ 0 \tag{18}$$

where Ψ is the multi-objective cost functional, $\{\omega_1, \omega_2, \omega_3\}$ are weighting coefficients satisfying $\sum_i \omega_i = 1$, ∇_{h_j} denotes the gradient operator with respect to thickness h_j, and $\mathcal{H}(\Psi)$ represents the Hessian matrix which must be positive definite at the optimal configuration to ensure a local minimum.

Haemoglobin-induced refractive index perturbation

The sensing mechanism relies on the concentration-dependent refractive index modulation of the aqueous analyte layer, where haemoglobin protein binding induces measurable optical path length changes detectable through resonance angle shifts.

$$n_N(\mathcal{C}_{Hb}, \lambda, T) = n_{H_2O}(\lambda, T) + \alpha_{Hb}(\lambda) \cdot \mathcal{C}_{Hb} + \beta_{Hb} \cdot \mathcal{C}_{Hb}^2 \tag{19}$$

$$n_{H_2O}(T) = n_{H_2O}(T_0) - \gamma_{thermo}(T - T_0) \; where \; \gamma_{thermo} \approx 1.0 \times 10^{-4} \; °C^{-1} \tag{20}$$

$$\tilde{n}_N = n_N + i\kappa_N = n_N + i\frac{\alpha_{abs}\lambda_0}{4\pi} \tag{21}$$

$$\Delta\theta_{res}(\mathscr{C}_{Hb}) = \mathfrak{S}_\theta \cdot \Delta n_N = \mathfrak{S}_\theta \cdot \alpha_{Hb} \cdot \Delta \mathscr{C}_{Hb} \tag{22}$$

$$\mathcal{C}_{Hb} = \frac{\Delta\theta_{res}}{\mathfrak{S}_\theta \cdot \alpha_{Hb}} = \frac{\theta_{measured} - \theta_{baseline}}{\mathfrak{S}_\theta \cdot \alpha_{Hb}} \tag{23}$$

where $n_N(\mathcal{C}_{Hb}, \lambda, T)$ is the refractive index of the sensing medium as a function of haemoglobin concentration $\mathcal{C}_{Hb}$ (g/dL), wavelength λ, and temperature T, n_{H_2O} is the refractive index of water at reference temperature T_0, α_{Hb} and β_{Hb} are the first and second-order concentration coefficients respectively, γ_{thermo} is the thermo-optic coefficient, κ_N is the extinction coefficient, α_{abs} is the absorption coefficient, and the measured resonance angle shift $\Delta\theta_{res}$ enables quantitative determination of haemoglobin concentration through the inverse relation.

Fresnel boundary conditions and interface physics

The electromagnetic boundary conditions at each heterointerface are governed by Fresnel coefficients that determine amplitude and phase modifications of propagating and evanescent waves, ensuring continuity of tangential field components across material discontinuities.

$$\rho_{j,j+1}^{(p)} = \frac{\varsigma_{j+1} - \varsigma_j}{\varsigma_{j+1} + \varsigma_j} = \frac{\tilde{n}_{j+1}^2 \cos\ \theta_j - \tilde{n}_j^2 \cos\ \theta_{j+1}}{\tilde{n}_{j+1}^2 \cos\ \theta_j + \tilde{n}_j^2 \cos\ \theta_{j+1}} \tag{24}$$

$$\tau_{j,j+1}^{(p)} = \frac{2\varsigma_j}{\varsigma_{j+1} + \varsigma_j} = \frac{2\tilde{n}_j \tilde{n}_{j+1} \cos\ \theta_j}{\tilde{n}_{j+1}^2 \cos\ \theta_j + \tilde{n}_j^2 \cos\ \theta_{j+1}} \tag{25}$$

$$\tilde{n}_j \sin\ \theta_j = \tilde{n}_{j+1} \sin\ \theta_{j+1} = n_0 \sin\ \theta_0 = \mathfrak{k}_{\|}^{(inv)} \tag{26}$$

$$\cos\ \theta_j = \sqrt{1 - \frac{n_0^2 \sin^{\,2}\theta_0}{\tilde{n}_j^2}} = \frac{\sqrt{\tilde{n}_j^2 - n_0^2 \sin^{\,2}\theta_0}}{\tilde{n}_j} \tag{27}$$

$$|\,\rho_{j,j+1}^{(p)}\,|^2 + \frac{\Re[\varsigma_{j+1}]}{\Re[\varsigma_j]}\,|\,\tau_{j,j+1}^{(p)}\,|^2 = 1\,(\text{Energy conservation}) \tag{28}$$

where $\rho_{j,j+1}^{(p)}$ and $\tau_{j,j+1}^{(p)}$ are the complex Fresnel reflection and transmission coefficients for p-polarised light at the interface between layers j and j + 1, θ_j and θ_{j+1} are the propagation angles in respective media satisfying Snell's law, $\mathfrak{k}_{\|}^{(inv)}$ is the conserved tangential wavevector component (invariant across all interfaces), and the energy conservation relation ensures physical consistency of the electromagnetic field solution.

Plasmonic absorption and quality factor

The resonance characteristics are fundamentally limited by intrinsic damping mechanisms in metallic and lossy dielectric layers, with the quality factor quantifying the trade-off between field confinement and dissipative losses.

$$\mathcal{A}(\theta, \omega) = 1 - \mathcal{R}_p(\theta, \omega) - \mathcal{T}_p(\theta, \omega) \approx 1 - \mathcal{R}_p(\theta, \omega) \tag{29}$$

$$\Gamma_{damp}^{(SPP)} = \Im[\mathfrak{k}_{\|}^{(SPP)}] = \frac{\omega}{c}\Im\left[\sqrt{\frac{\tilde{\varepsilon}_m \tilde{\varepsilon}_d}{\tilde{\varepsilon}_m + \tilde{\varepsilon}_d}}\right] \tag{30}$$

$$\mathcal{Q}_{plasmon} = \frac{\Re[\mathfrak{k}_{\|}^{(SPP)}]}{2\Im[\mathfrak{k}_{\|}^{(SPP)}]} = \frac{\Re[\mathfrak{k}_{\|}^{(SPP)}]}{2\Gamma_{damp}^{(SPP)}} \tag{31}$$

$$\mathcal{P}_{diss} = \int_{\text{all layers}} \frac{1}{2}\omega\varepsilon_0\varepsilon_j''\,|\,\mathbb{E}_j(\zeta)|^2\,dV \tag{32}$$

$$\Omega_{FWHM} \propto \frac{1}{\mathcal{Q}_{plasmon}} \propto \Gamma_{damp}^{(SPP)} \tag{33}$$

where $\mathcal{A}(\theta, \omega)$ represents the angle and frequency-dependent absorption, $\mathcal{T}_p$ is the transmitted intensity (negligible for optically thick metal layers), $\Gamma_{damp}^{(SPP)}$ quantifies the damping rate of surface plasmon polaritons, $\mathcal{Q}_{plasmon}$ is the plasmonic quality factor representing the number of oscillation cycles before decay, $\mathcal{P}_{diss}$ denotes the total dissipated power density with ε_j'' being the imaginary part of the permittivity in layer j, and the inverse proportionality between quality factor and resonance width establishes the fundamental sensitivity-sharpness trade-off in plasmonic biosensing.

From a practical deployment perspective, the proposed sensor is compatible with standard prism-coupled SPR interrogation systems operating in angular modulation mode. The sensor response is wavelength-dependent, with optimal operation occurring near the design wavelength used in simulations. Alignment tolerances are comparable to conventional Kretschmann-based SPR sensors, where angular resolution directly governs detection limits.

Environmental noise sources such as temperature fluctuations and mechanical vibrations primarily influence resonance stability and can be mitigated through thermal control and differential referencing. Furthermore, the incorporation of graphene and ZrN layers enhances chemical robustness by protecting the underlying silver layer against oxidation, thereby improving long-term operational stability.

Results and discussion

The performance of the proposed sensor was optimised through finite element method (FEM) simulations in COMSOL Multiphysics, focusing on the synergistic effect of the silver (Ag), carbon nanotube (CNT), and graphene layers. The thickness of the Ag thin film was initially varied from 25 nm to 49 nm in steps of 4 nm to identify the optimal condition for excitation of surface plasmon polaritons (SPPs). As illustrated in Figure 3a,b, the maximum reflectance remained stable between 99.919% and 99.938%. However, the minimum reflectance—representing the resonance dip—showed high sensitivity to thickness, decreasing sharply from 87.569% to a minimum of 23.373%. The colour map in Figure 4a highlights this evolution, showing that the resonance depth is highly dependent on the damping and coupling efficiency of the silver layer. This suggests that near 49 nm, the sensor achieves a state closer to critical coupling, which is essential for maximising sensitivity. To enhance the light-matter interaction and the biosensing surface area, the CNT layer thickness was swept from 2 nm to 14 nm (2 nm increments). While the peak reflectance remained consistently high (99.941%–99.948%), a subtle but critical reduction in the reflectance minimum (from 23.953% to 23.368%) was observed, as shown in Figure 3c–d. The colour plot in Figure 4b indicates that the CNT layer acts as a dielectric buffer that slightly shifts the resonance phase without significantly increasing parasitic absorption. This improvement in modulation depth suggests that the CNT layer not only provides more binding sites but also refines the optical confinement at the interface. Finally, the impact of the graphene overlayer was investigated by varying its thickness from 0.2 nm to 1.4 nm (corresponding to approximately 1 to 4 layers). As presented in Figure 3e,f, increasing the graphene thickness led to a pronounced deepening of the resonance dip, with the minimum reflectance dropping to 21.711%. Although a minor reduction in maximum reflectance was noted (from 99.950% to 99.927%), the overall resonance contrast was significantly enhanced. The colour map in Figure 4c reveals that the graphene layer facilitates a tunable interaction between the plasmonic Ag layer and the analyte, effectively concentrating the electromagnetic field at the sensor's surface.

Table 1 summarises the reflectance behaviour of the proposed sensor as the thicknesses of Ag, CNT, and graphene layers are varied. It shows the corresponding maximum and minimum reflectance values, highlighting how layer tuning influences resonance depth and optical response.

After attaining the optimised sensor design through systematic parameter tuning, we employed it for the quantitative detection of haemoglobin concentrations in aqueous solutions. For this comprehensive study, haemoglobin concentration was systematically varied across a clinically relevant range from 10 g/L to 40 g/L in uniform increments of 10 g/L. These concentrations correspond to refractive indices of 1.33,

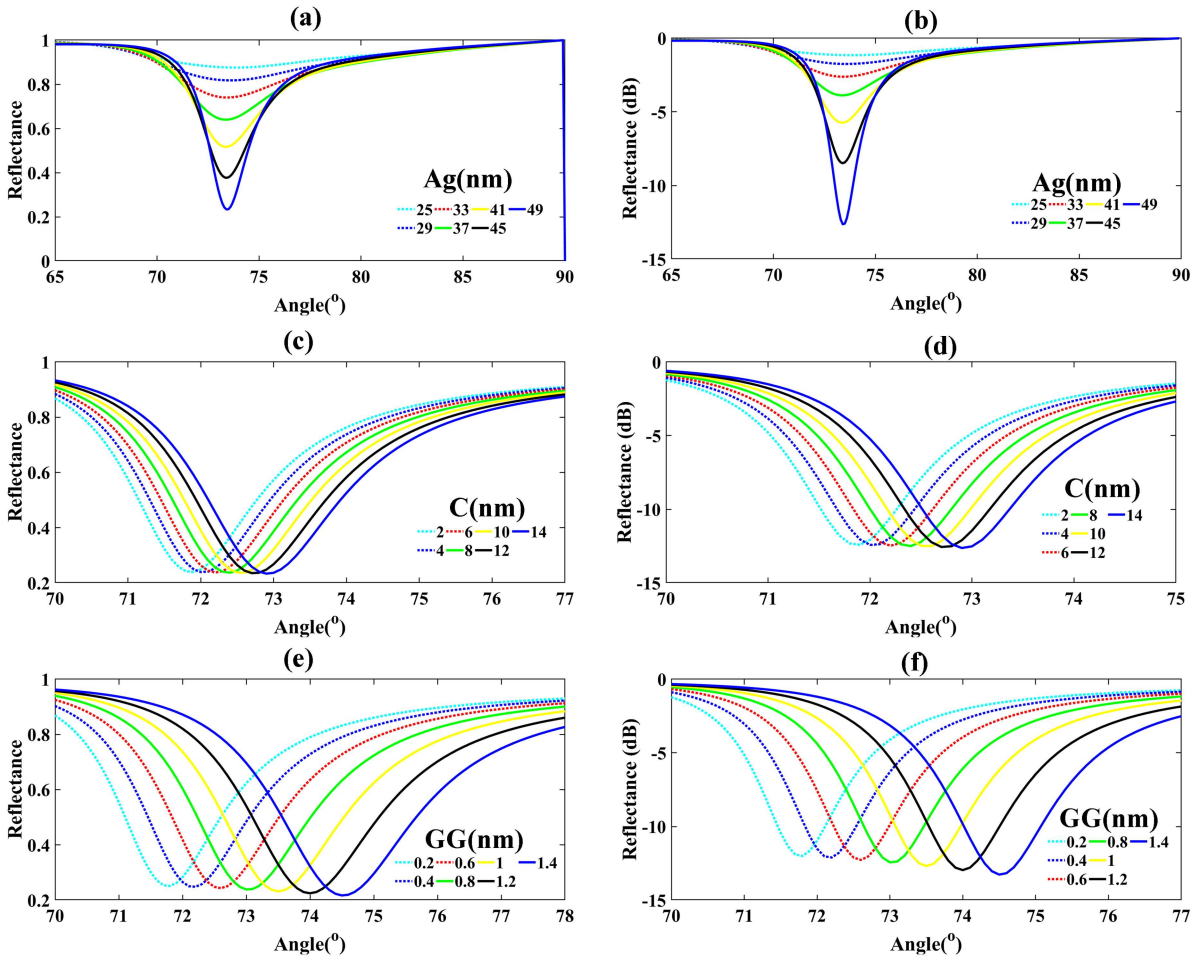

Figure 3. Reflectance spectra of the proposed sensor for varying layer thicknesses. (a,b) Ag layer thickness varied from 25 nm to 49 nm, showing maximum and minimum reflectance values in linear scale (a) and in dB scale (b). (c,d) CNT layer thickness varied from 2 nm to 14 nm, with reflectance in linear scale (c) and dB scale (d). (e,f) Graphene layer thickness varied from 0.2 nm to 1.4 nm, showing reflectance in linear scale (e) and dB scale (f). Each set illustrates the effect of layer thickness on the sensor's optical response and resonance depth.

1.35, 1.36, 1.38, and 1.40, respectively, which were determined based on established optical properties of haemoglobin solutions. The correlation between haemoglobin concentration and refractive index is well-documented in the literature and forms the foundation of our optical detection mechanism. The sensor's optical response to these refractive index variations was meticulously analysed by recording the reflectance spectra across the wavelength range of interest under identical experimental conditions. The spectral data were collected with high resolution to capture subtle changes in the resonance characteristics. The comprehensive results are presented in Figure 5a,b, where Figure 5a displays the reflectance in percentage form and Figure 5b presents the same data in decibel (dB) scale for enhanced visualisation of dynamic range. Analysis of the spectral data revealed distinct trends in both the maximum and minimum reflectance values. The maximum reflectance values observed at off-resonance wavelengths were 99.932%, 99.916%, 99.901%, 99.840%, and 99.534% for the five concentrations tested, showing a gradual decrease with increasing haemoglobin concentration. More notably, the minimum reflectance values—occurring at the resonance wavelength—decreased dramatically from 69.450% at 10 g/L to 12.896% at 40 g/L. This substantial reduction reflects a progressive deepening and sharpening of the resonance dip with increasing haemoglobin concentration, indicating enhanced light-matter interaction at the sensor interface. The resonance dip depth increased from approximately 30.5% to 87.1% across this concentration range, demonstrating exceptional sensitivity. Figure 5b presents the same reflectance data in dB scale (calculated as $10 \times \log_{10}(R)$, where R is the reflectance), which provides a clearer and more

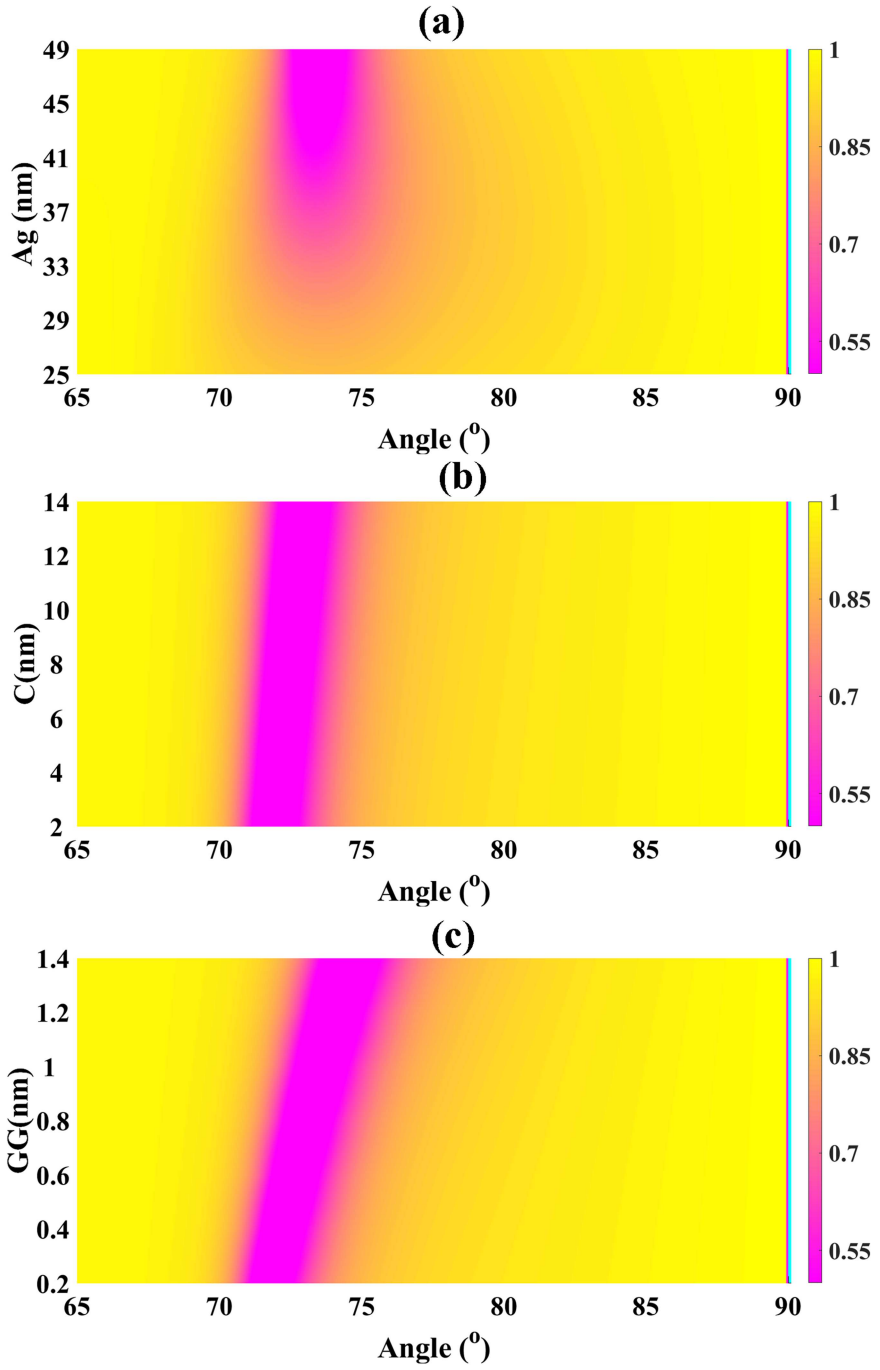

Figure 4. Colour maps of reflectance for the proposed sensor under parametric layer variations. (a) Ag layer thickness variation from 25 nm to 49 nm, (b) CNT thickness variation from 2 nm to 14 nm, and (c) graphene thickness variation from 0.2 nm to 1.4 nm. The plots visualise the progressive changes in resonance depth and reflectance spectrum, providing insight into the sensitivity and tunability of the sensor.

Table 1. Reflectance characteristics of the proposed sensor for different layer thicknesses.

Layer	Thickness range	Step (nm)	Max reflectance (%)	Min reflectance (%)
Ag	25–49	4	99.934, 99.924, 99.919, 99.920, 99.924, 99.931, 99.938	87.569, 81.766, 74.012, 63.985, 51.683, 37.659, 23.373
CNT	2–14	2	99.948, 99.947, 99.946, 99.945, 99.944, 99.942, 99.941	23.953, 23.931, 23.787, 23.724, 23.704, 23.553, 23.368
Graphene	0.2–1.4	0.2	99.950, 99.948, 99.945, 99.942, 99.938, 99.933, 99.927	25.120, 24.811, 24.350, 23.893, 23.208, 22.489, 21.711

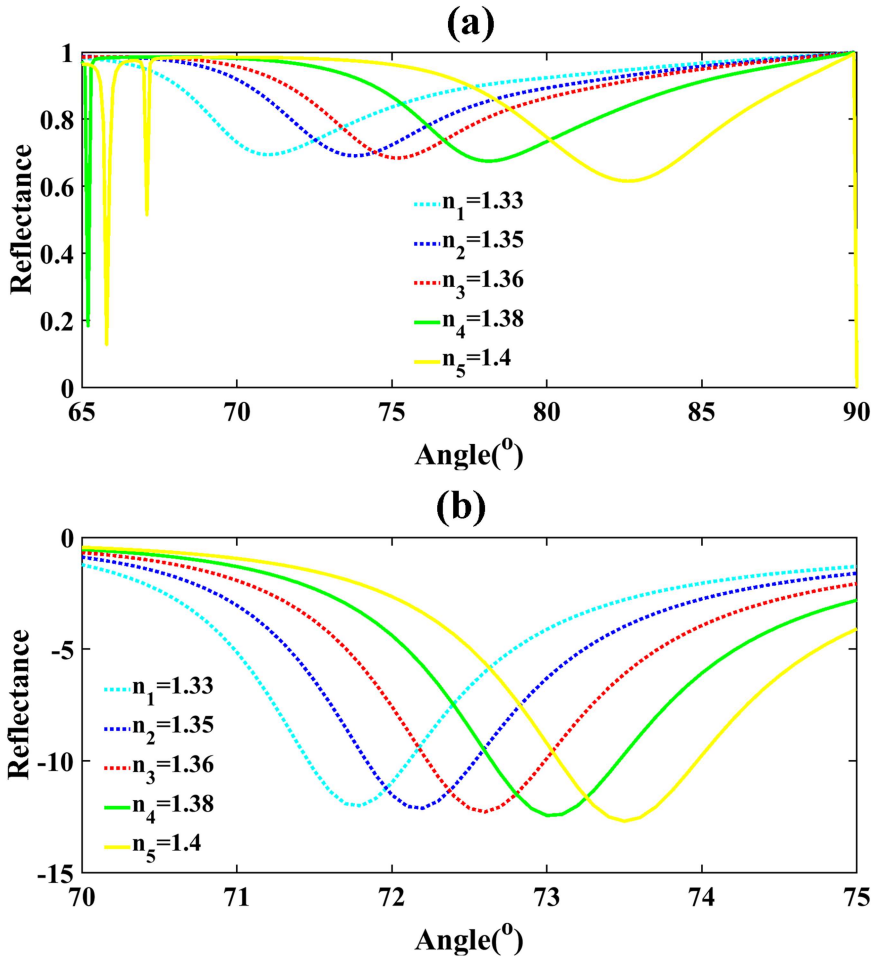

Figure 5. Reflectance response of the optimised sensor for varying haemoglobin concentrations. (a) Maximum and minimum reflectance values for haemoglobin concentrations ranging from 10 g/L to 40 g/L. (b) The same reflectance data presented in dB scale, highlighting the progressive deepening of the resonance dip with increasing haemoglobin concentration.

intuitive representation of the modulation depth and signal contrast. The logarithmic scale better emphasises the dynamic range of the sensor response and facilitates comparison across different measurement conditions. The dB representation is particularly valuable for assessing sensor performance in terms of signal-to-noise ratio and detection limits.

It is noted that SPR inherently responds to refractive index variations and does not provide molecular specificity in the absence of surface functionalization. In practical implementations, selective haemoglobin detection would be achieved through immobilisation of Hb-specific receptors, antibodies, or aptamers on the graphene surface. Such functionalization strategies are well established and enable discrimination against non-specific plasma proteins in complex biological fluids.

We have also evaluated the relationship between the resonance angle and the refractive index (RI), as illustrated in Figure 6. In this analysis, the resonance angle exhibits a generally linear dependence on the RI, which can be described by the following linear regression equation:

$$\theta(^\circ) = -115.0685\ \mathrm{RI} + 227.1534 \tag{34}$$

where θ represents the resonance angle in degrees and RI is the refractive index of the analyte. The negative slope indicates that the resonance angle decreases as the refractive index increases, a trend consistent with the behaviour of surface plasmon resonance (SPR)-based sensors. The goodness of fit, quantified by the R-squared value of 0.86604, suggests a moderate correlation between the resonance angle

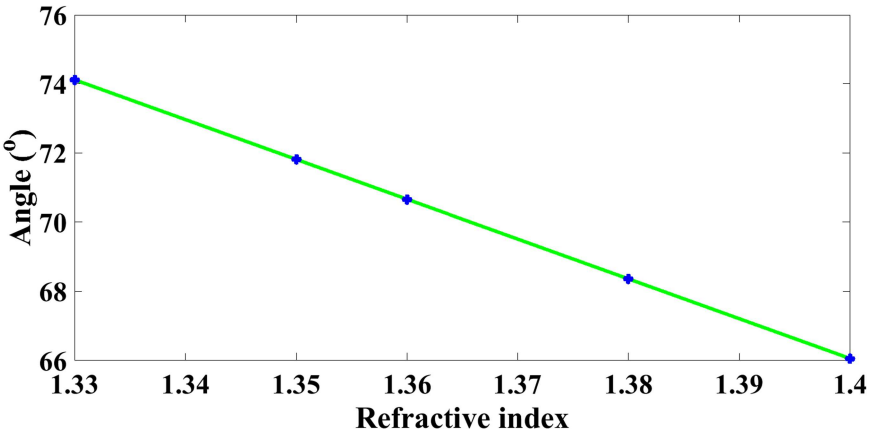

Figure 6. Variation of the resonance angle (θ) with refractive index (RI) of the analyte. The relationship is approximately linear, with the fitted regression line described by θ (°) = −115.0685 RI + 227.1534 (R^2 = 0.46604).

and RI. Although the relationship is approximately linear, some deviations are observed, likely due to simulation variations, non-idealities in the sensing interface, or nonlinear effects at higher RI values.

The fitted relationships between resonance parameters and refractive index or analyte concentration serve as calibration curves rather than fundamental sensing laws. In practical operation, the sensor is first calibrated using known concentrations, and the resulting fitted relationship is then used to infer the concentration of an unknown sample from the measured resonance shift. This approach is consistent with conventional SPR-based biosensing protocols.

Figure 7a–c presents the spatial distribution of the electric field norm as a function of arc length (extending to 4.5 μm) for three distinct incident angles: 68.345° (Figure 7a), 70.913° (Figure 7b), and 79.234° (Figure 7c). A comparative analysis of these distributions reveals several characteristic features that demonstrate the angular dependence of electromagnetic field localisation in the sensor structure.

In all three configurations, the electric field magnitude remains negligibly small ($|E| \approx 0$) throughout the initial portion of the arc (0 to approximately 2.5 μm), indicating minimal electromagnetic coupling and field penetration in this region. This behaviour is consistent with the propagation characteristics of the incident wave prior to encountering the resonant structure. At an arc length of approximately 3.0 μm, each angular configuration exhibits a pronounced, localised maximum in the electric field norm, reaching peak intensities on the order of 10^6 V/m. This dramatic field enhancement is attributed to resonant coupling at the metal-dielectric interface, where surface plasmon polaritons (SPPs) or localised surface plasmons are excited under phase-matching conditions. The spatial localisation of this peak suggests strong field confinement at a critical geometric feature—likely the prism-metal interface or a region of discontinuity in the multilayer stack.

The post-resonance field behaviour (arc length > 3.0 μm) exhibits marked angular dependence. For $\theta = 68.345°$ (Figure 7a), the electric field establishes oscillatory behaviour with a mean amplitude of approximately 0.5×10^5 V/m and moderate fluctuation envelope. At $\theta = 70.913°$ (Figure 7b), which corresponds more closely to the resonance angle, the oscillation amplitude is reduced to approximately 5×10^4 V/m while maintaining comparable spatial periodicity, suggesting more efficient energy coupling into the propagating surface mode. For $\theta = 79.234°$ (Figure 7c), the field exhibits larger-amplitude oscillations spanning the range of 2×10^4 to 7×10^4 V/m, indicative of beating patterns or interference effects arising from phase mismatch conditions away from optimal resonance. These angular-dependent variations in both the peak field enhancement and the subsequent spatial field distribution underscore the critical role of incident angle in determining the electromagnetic field configuration within the sensor. The observed sensitivity to angular positioning confirms that precise control of the excitation geometry is essential for optimising sensor performance, as the magnitude and spatial extent of field enhancement directly govern the sensitivity to refractive index changes in the sensing medium. Figure 8a–c demonstrates the same results in terms of colour plots.

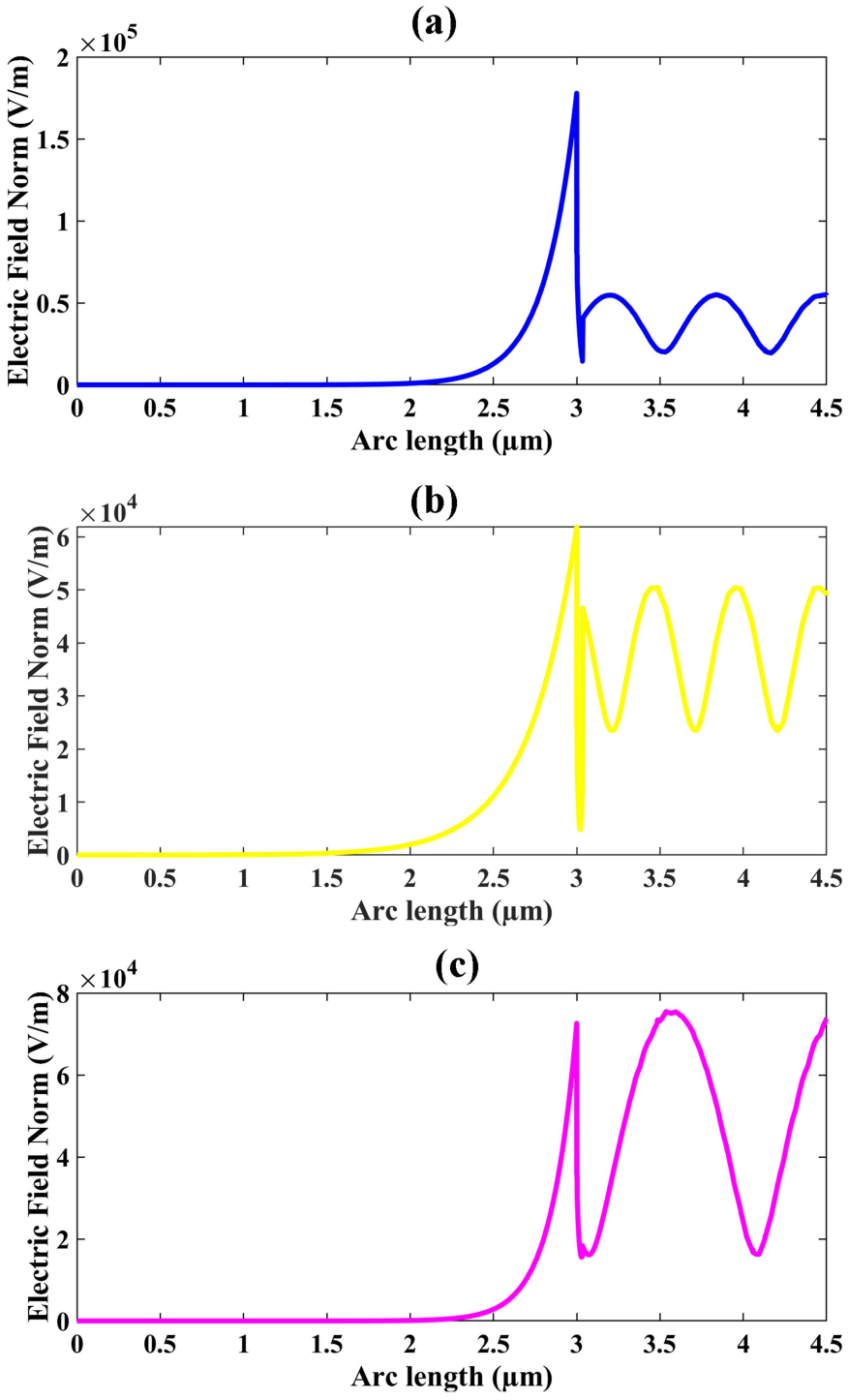

Figure 7. a–c presents the spatial distribution of the electric field norm as a function of arc length (extending to 4.5 μm) for three distinct incident angles: 68.345° (Figure 7a), 70.913° (Figure 7b), and 79.234° (Figure 7c).

Table 2 and Figure 9 summarises the performance of the proposed sensor for haemoglobin detection across different refractive indices (RI) ranging from 1.33 to 1.4 RIU. The corresponding resonance angles (θ) vary between 65.2° and 75.2°, with the largest angular shift observed at 75.2° for an RI of 1.36 RIU. The angular variation, $\Delta\theta$, spans from 0.6° to 10°, while the RI changes (Δn) are between 0.01 and 0.02 RIU. The sensitivity (S) of the sensor shows a wide range, from 30°/RIU up to 500°/RIU, indicating the sensor's differential responsiveness depending on the analyte concentration. The full-width at half maximum (FWHM) remains relatively stable around 5.399°–5.430°, demonstrating consistent resonance peak

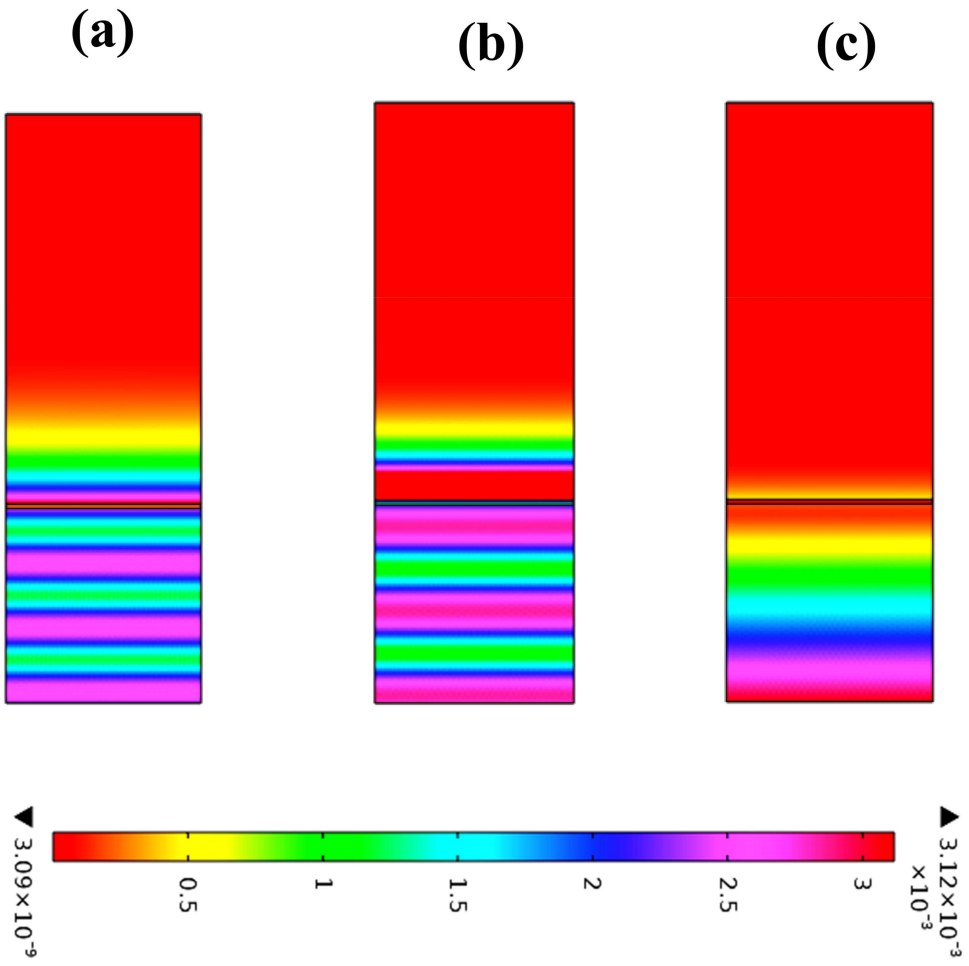

Figure 8. a–c presents the colour plots spatial distribution of the electric field norm as a function of arc length (extending to 4.5 µm) for three distinct incident angles: 68.345° (Figure 7a), 70.913° (Figure 7b), and 79.234° (Figure 7c).

Table 2. Performance metrics of the proposed haemoglobin sensor for different refractive indices (RI).

θ (°)	71	73.8	75.2	65.2	65.8
n(RIU)	1.33	1.35	1.36	1.38	1.4
dθ (°)		2.8	1.4	10	0.6
dn(RIU)		0.02	0.01	0.02	0.02
S(°/RIU)		140	140	500	30
FWHM(°)	5.399	5.398	5.410	5.420	5.430
FOM(RIU^{-1})		25.936	25.878	92.251	5.525
Q		25.936	25.878	92.251	5.525
DL		0.030	0.036	0.006	0.209
DR	30.556	31.764	32.331	28.006	28.237
SR		4.240	5.057	3.100	6.279
SNR		0.519	0.259	1.845	0.110
X		0.733	0.436	1.907	0.231

sharpness across the measured range. The figure of merit (FOM) and quality factor (Q) both peak at 92.251 for the RI of 1.36, highlighting the optimal sensing performance at this point. Additional performance parameters reflect the detection capability and reliability of the sensor. The detection limit (DL) is lowest at 0.006 RIU for an RI of 1.36, suggesting the highest precision at this concentration, while the dynamic range (DR) fluctuates between 28.006° and 32.331°, indicating the measurable angle span. The sensor's sensitivity ratio (SR) varies from 3.100 to 6.279, and the signal-to-noise ratio (SNR) ranges from 0.110 to 1.845, with the highest SNR also observed at 1.36 RIU. Finally, the parameter X, representing normalised sensor response, shows peak performance at 1.907 for the same RI value, consistent with the highest sensitivity, FOM, and Q, confirming that the sensor exhibits maximum detection efficiency at an RI of 1.36.

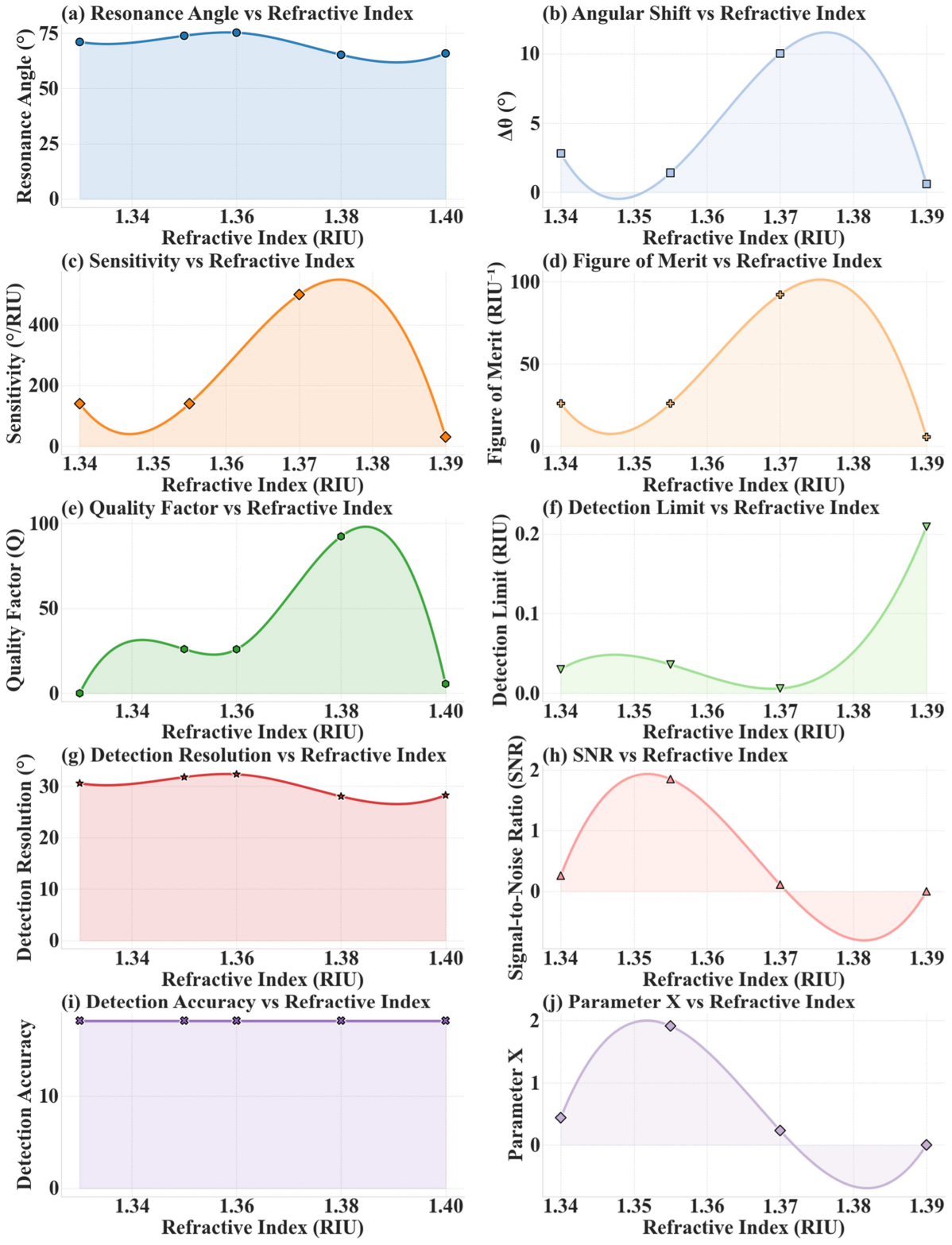

Figure 9. Performance analysis of the proposed haemoglobin sensor as a function of refractive index (RI).

Machine learning

Machine learning was employed as a surrogate modelling tool to efficiently predict the optical response of the SPR sensor under variations in graphene thickness (t_g) and analyte refractive index (n_a). The input feature vector $\mathbf{X} = [t_g, n_a]$ encapsulated both structural and environmental parameters, while the output

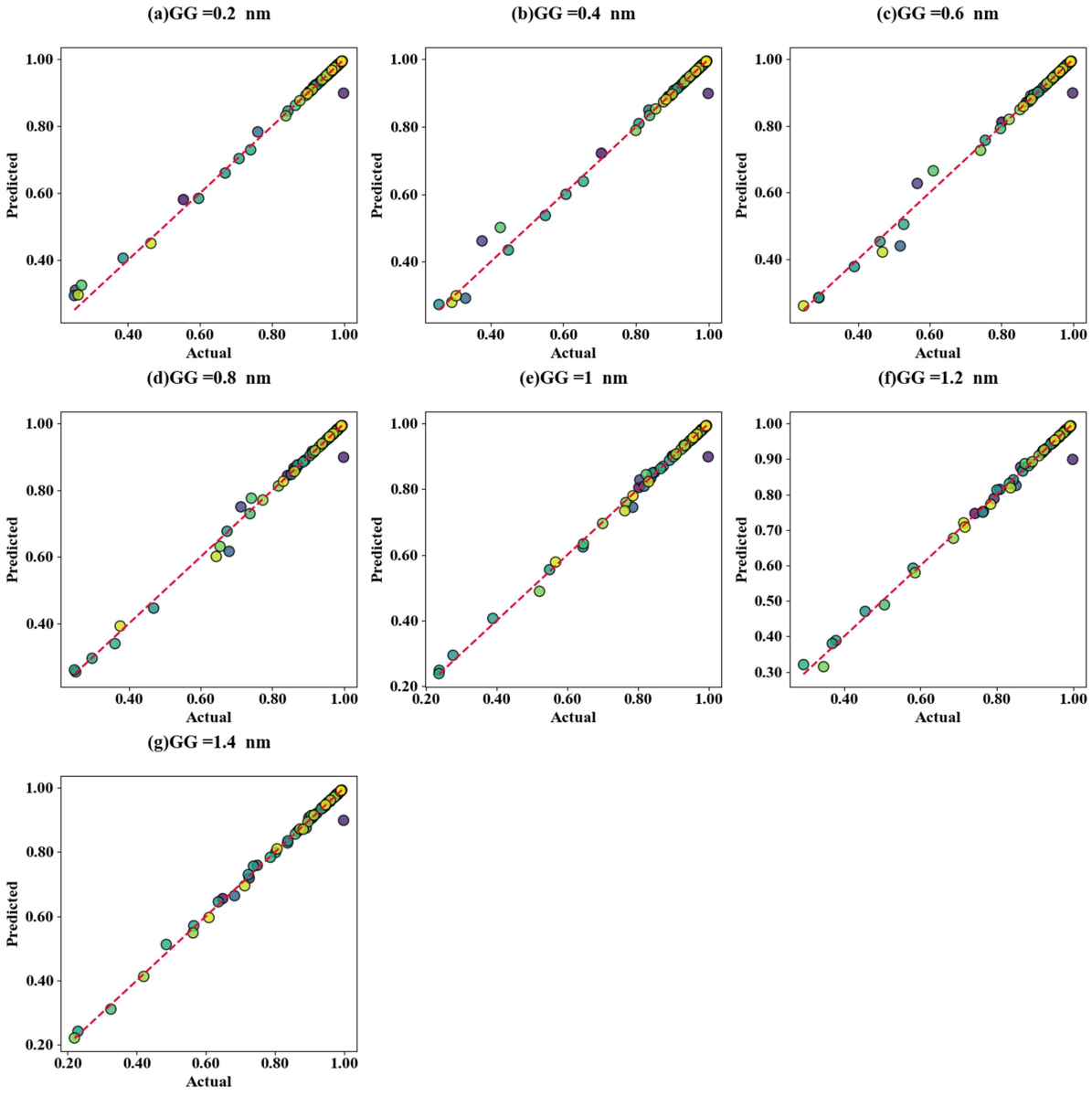

Figure 10. Scatter plots showing the predicted versus actual sensor response for different graphene thicknesses (0.2–1.4 nm), demonstrating the accuracy of the machine learning model in capturing thickness-dependent behaviour.

targets $\mathbf{Y} = [\theta_{res}, R(\theta)]$ represented the resonance angle shifts (θ_{res}) and angular reflectance spectra $R(\theta)$. The sensor's reflectance response is governed by the Fresnel equations for multilayer structures, expressed as

$$r_p = \frac{n_2 \cos\ \theta_1 - n_1 \cos\ \theta_2}{n_2 \cos\ \theta_1 + n_1 \cos\ \theta_2},\ R_p = |\ r_p\ |^2, \tag{35}$$

where r_p is the p-polarised reflection coefficient, R_p is the reflectance, and n_1, n_2 denote refractive indices of adjacent layers. The resonance condition satisfies

$$\mathrm{Re}[\beta_{SPP}] = k_0 n_{prism} \sin \theta_{res},\ \beta_{SPP} = k_0 \sqrt{\frac{\varepsilon_m \varepsilon_a}{\varepsilon_m + \varepsilon_a}}, \tag{36}$$

with β_{SPP} being the surface plasmon polariton (SPP) propagation constant, $k_0 = 2\pi/\lambda$ the free-space wavenumber, ε_m the metal permittivity, and ε_a the analyte permittivity. The K-nearest neighbour

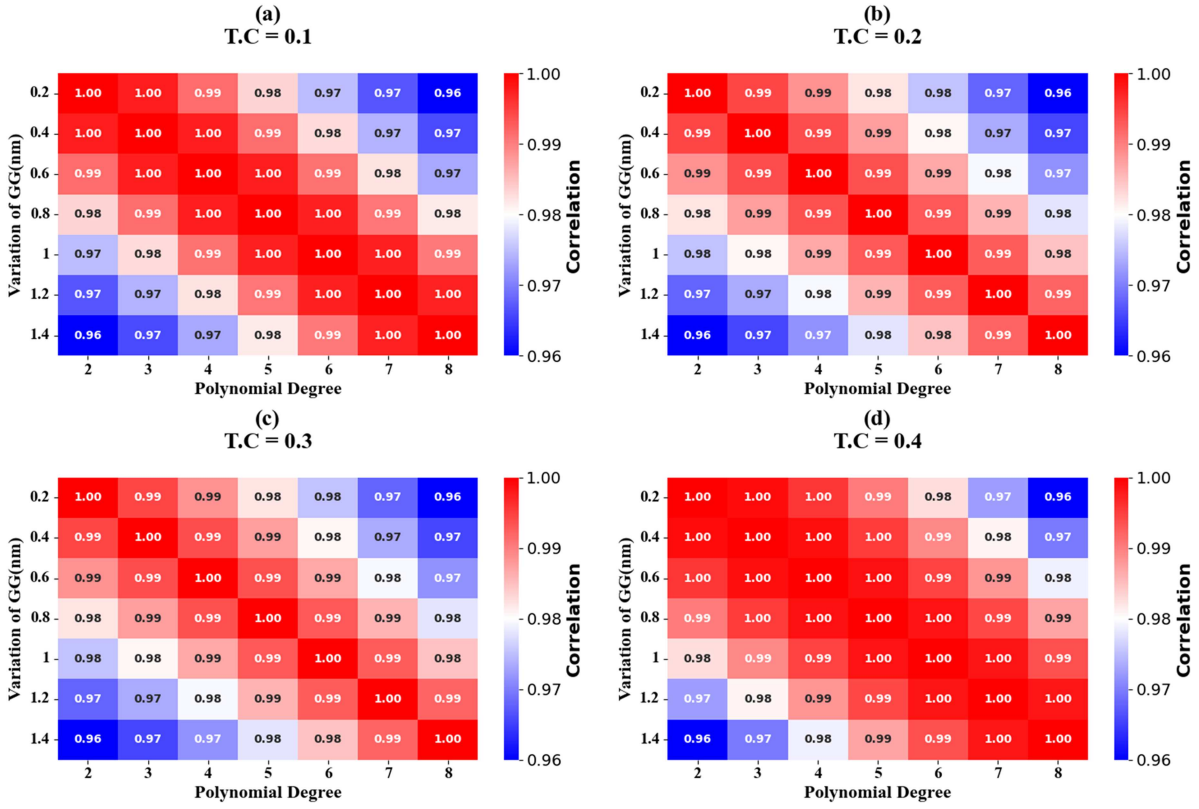

Figure 11. Heat map representations of sensor response as a function of graphene thickness, illustrating the model's ability to predict variations and trends across the thickness range.

(KNN) regressor was selected due to its ability to capture the nonlinear mapping $\mathbf{X} \mapsto \mathbf{Y}$ without assuming an explicit parametric form, making it particularly suitable for low-dimensional, physics-driven datasets. The KNN prediction is defined as

$$\hat{\mathbf{Y}}(\mathbf{X}_{\text{new}}) = \frac{1}{K} \sum_{i \in \mathcal{N}_K(\mathbf{X}_{\text{new}})} \mathbf{Y}_i, \tag{37}$$

where $\mathcal{N}_K(\mathbf{X}_{\text{new}})$ denotes the set of K nearest neighbours of the input $\mathbf{X}_{\text{new}}$.

The dataset obtained from full-wave electromagnetic simulations was partitioned into training and validation subsets using an 80/20 split. Model performance was quantified through multiple metrics: mean squared error (MSE), root mean squared error (RMSE), mean absolute error (MAE), and coefficient of determination (R^2):

$$\text{MSE} = \frac{1}{N}\sum_{i=1}^{N}(\hat{y}_i - y_i)^2,\ \text{RMSE} = \sqrt{\text{MSE}},\ \text{MAE} = \frac{1}{N}\sum_{i=1}^{N}|\hat{y}_i - y_i|,\ R^2 = 1 - \frac{\sum_i (\hat{y}_i - y_i)^2}{\sum_i (y_i - \bar{y})^2}, \tag{38}$$

where y_i and $\hat{y}_i$ are the simulated and predicted values, respectively, and $\bar{y}$ is the mean of the simulated data. Across all tested ranges, the ML model achieved consistently low MSE, RMSE, and MAE values, with $R^2 > 0.99$, indicating excellent predictive fidelity. By accurately approximating the SPR sensor's electromagnetic behaviour, this ML framework dramatically reduces computational expense compared to repeated full-wave simulations, enabling rapid multi-parameter optimisation. Consequently, the surrogate model functions as an integral component of the sensor design pipeline, facilitating iterative refinement and sensitivity enhancement, rather than being a mere post-processing tool.

Table 3. The impact of varying graphene thickness on the sensor's response.

Thickness (nm)	MSE	RMSE	R^2	MAE
0.2	0.000281	0.016763	0.992081	0.005991
0.4	0.000346	0.018590	0.990335	0.006213
0.6	0.000351	0.018742	0.989617	0.006576
0.8	0.000272	0.016492	0.991751	0.006085
1.0	0.000213	0.014611	0.993155	0.005627
1.2	0.000195	0.013958	0.993216	0.005590
1.4	0.000177	0.013315	0.994482	0.005100

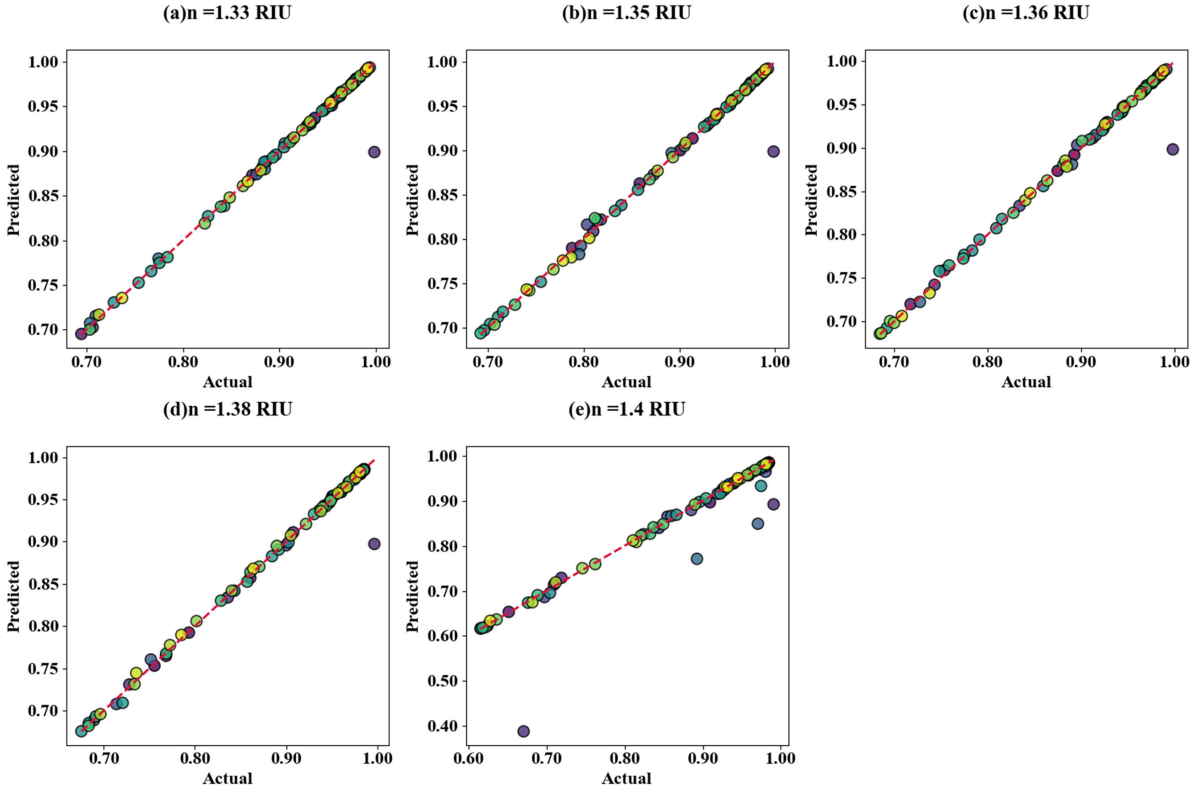

Figure 12. Scatter plots depicting the predicted versus actual sensor response for varying analyte refractive indices (1.33–1.40), highlighting the machine learning model's performance in refractive index prediction.

We have also evaluated the effectiveness of machine learning (ML) models in predicting the behaviour of the proposed sensor design under different parameter variations. Specifically, two key factors were considered: graphene thickness and refractive index (RI) of the analyte.

The impact of varying graphene thickness on the sensor's response was analysed using scatter plots (Figure 10a–g) and corresponding heat map visualisations (Figure 11a–d).

From the results, it is evident that the ML model achieves high accuracy across all thicknesses, as indicated by consistently low mean squared error (MSE) and mean absolute error (MAE) values, along with R^2 values exceeding 0.99 (Table 3). This demonstrates that the model can reliably predict the sensor's behaviour as the graphene layer is varied. Notably, the prediction accuracy slightly improves with increasing thickness, suggesting the model captures subtle effects of the thicker graphene layer on sensor performance Figure 11.

Similarly, the model was assessed for its ability to predict sensor responses to changes in the analyte's refractive index. Scatter plots (Figure 12a–e) and heat maps (Figure 13a–d) illustrate how the predicted sensor behaviour aligns with the actual data. The ML performance metrics for various RI values are summarised below:

The results indicate excellent predictive capability for RI values up to 1.38, with low error metrics and R^2 values above 0.98. For RI = 1.40, the prediction performance slightly decreases, as reflected by the

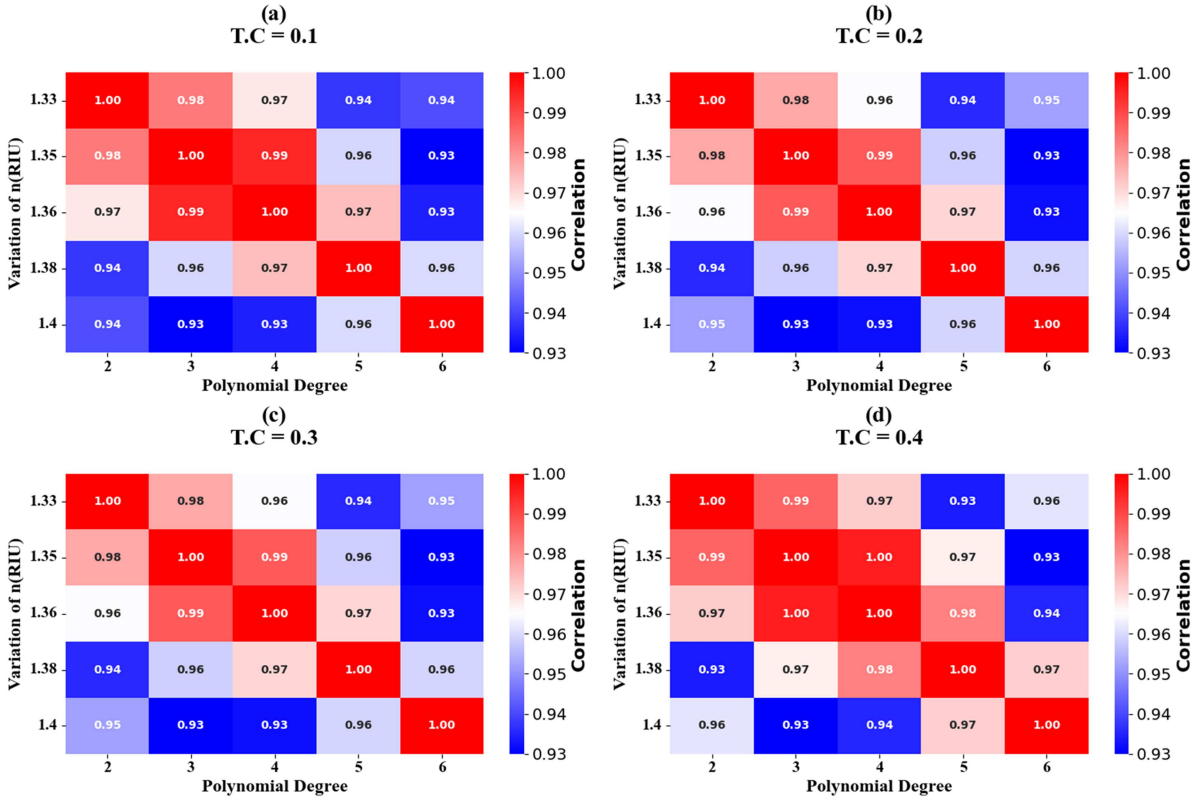

Figure 13. Heat map visualisations of sensor response across different refractive indices, showing the variation trends and effectiveness of the ML model in predicting RI-dependent behaviour.

Table 4. The impact of varying graphene thickness on the sensor's response.

RIs	MSE	RMSE	R^2	MAE
1.33	0.000135	0.011604	0.982476	0.002641
1.35	0.000141	0.011880	0.984017	0.003173
1.36	0.000138	0.011765	0.985335	0.003089
1.38	0.000139	0.011780	0.986248	0.003241
1.40	0.001610	0.040130	0.895437	0.011461

Table 5. Comparative analysis of plasmonic and 2D-material-based sensors, showing their sensitivity, target application, and structural configuration.

Ref	Sensitivity(o/RIU)	Application	Structrure
[54]	269.58 deg/RIU	Cervical cancer	Ag/$BaTiO_3$/BP
[55]	194.12 degree/RIU	Glucose detection	Old, molybdenum disulphide (MoS2), h-BN (hexagonal boron nitride), and graphene.
[56]	416.85 deg/RIU	Cancer	*N*-FK51A/Ag/AlON/BlueP
[57]	315.74°/RIU	Glucose	Ag and ZrN
[58]	150.42 deg/RIU	Colorectal cancer	Silver, Nickel, and Black Phosphorous
[59]	357.14°/RIU	Skin cancer	Kretchmann configuration
Proposed	500°/RIU	Haemoglobin detection	BK-7 prism/graphene/silver/carbon nanotube/biosample stack

higher MSE and lower R^2 (Table 4). This is likely due to increased nonlinearity or reduced training data coverage in this RI range. Overall, the ML approach demonstrates robust performance and provides a rapid, reliable method for predicting sensor responses across a wide range of design parameters.

Table 5 compares the sensitivity, application, and structure of various plasmonic and 2D-material-based sensors. Sensitivities range from around 150°/RIU for colorectal cancer detection to over 400°/RIU for cancer detection, with applications including glucose, skin, and cervical cancer sensing. The proposed sensor achieves the highest sensitivity of 500°/RIU for haemoglobin detection using a layered BK-7 prism/graphene/silver/carbon nanotube/biosample structure, indicating superior performance compared to

existing designs. Compared to direct numerical simulations and traditional regression fitting, the ML-assisted framework demonstrates superior capability in capturing nonlinear dependencies between graphene thickness, refractive index, and resonance behaviour. While linear regression provides local approximations, the ML model generalises across the design space with consistently low prediction error, enabling rapid performance evaluation without repeated full-wave computation.

Conclusion

This study presents a comprehensive theoretical and numerical investigation of a high-performance multilayer SPR biosensor tailored for haemoglobin detection. By integrating graphene and zirconium nitride with a silver plasmonic layer in a Kretschmann configuration, the proposed design successfully combines high sensitivity, sharp resonance characteristics, and enhanced chemical stability. Systematic thickness optimisation of the Ag, graphene, and CNT/ZrN layers reveals strong control over resonance depth and electromagnetic field confinement, leading to pronounced sensitivity enhancements across clinically relevant refractive-index ranges.The optimised sensor achieves a peak angular sensitivity of 500°/RIU, a high figure of merit exceeding 92 RIU^{-1}, and a low detection limit of 0.006 RIU, outperforming many previously reported plasmonic and 2D-material-based biosensors for biochemical sensing. Spatial field distribution analysis confirms strong plasmonic localisation at the sensing interface, directly underpinning the observed sensing performance. In addition, the incorporation of machine learning provides a powerful predictive framework for rapid evaluation of sensor behaviour under varying structural and analyte parameters, significantly reducing reliance on exhaustive parametric simulations.

Disclosure statement

No potential conflict of interest was reported by the author(s).

Funding

The authors are thankful to the Deanship of Graduate Studies and Scientific Research at Najran University for funding this work under the Growth Funding Programme grant code (NU/GP/SERC/13/XX-X). The authors are thankful to the Deanship of Graduate Studies and Scientific Research at the University of Bisha for supporting this work through the Fast-Track Research Support Programme. The authors extend their appreciation to the Deanship of Research and Graduate Studies at King Khalid University for funding this work through Large Research Project under grant number RGP2/301/46 and Princess Nourah Bint Abdulrahman University.

ORCID

William Ochen 0009-0009-7639-7917
Jonas Muheki 0000-0001-6666-2785

Data availability statement

The data supporting the findings of this study are available from the corresponding author upon reasonable request.

Ethical approval

Not applicable.

References

[1] Sharma A, Biswas L, Annu, et al. Therapeutic approaches of silver nanoparticles against pancreatic cancer, or.niscpr.res.in, 2026. Accessed: Jan. 3, 2026. [Online]. https://or.niscpr.res.in/index.php/IJBB/article/view/21585
[2] Dada M, Popoola A, Adeyoye A. Polymer nanocomposites In: Functionalized carbon nanotube nanocomposites for biosensor and gas sensor application. Woodhead Publishing; 2026. pp. 363–389. Accessed: Jan. 3, 2026. [Online]. doi: 10.1016/B978-0-443-13756-3.00004-X

[3] Neupane G, Salaria RK. Improving SERS sensitivity via hot spots and control of molecular orientation, pubs.rsc.org, 2026. Accessed: Jan. 3, 2026. [Online]. https://pubs.rsc.org/en/content/articlehtml/2025/tc/d5tc02771c
[4] Hussain A, Altamimi M, Webster TJ. Detection, and treatment, and undefined. In: Harnessing the application of nano sensors for the detection and treatment of mycobacterium tuberculosis. World Scientific; 2026. doi: 10.1142/14450
[5] Meshari A, Wekalao J, Patel SK, et al. Enhanced sensing efficiency of ultra-narrow band graphene-based surface plasmon resonance refractive index sensor for biochemical applications and environmental monitoring. Plasmonics. 2024;20:1273–1284.
[6] Muheki J, Elsayed HA, Alfassam HE, et al. Design and optimization of a hybrid Graphene–Gold–Silver terahertz metasurface biosensor for high-sensitivity sperm detection with machine learning for behavior prediction. In: J Muhek, Elsayed HA, Alfassam HE, Ochen W, Rajakannu A, Mehaney A, Wekalao J, editors. J Electron Mater. Springer; 2025. p. 2348–2371. doi: 10.1007/S11664-025-12520-3
[7] Elsayed H, Wekalao J, Messaoudi M, et al. Advanced surface plasmon resonance biosensor for glucose detection using ZnSe/WS2/graphene/BaTiO3 multilayer architecture: electromagnetic modeling and machine learning performance optimization. In: Elsayed HA, Wekalao J, Messaoudi M, Mehaney A, Muheki J, Solouma E, Rajakannu A, editors. Microchem J. Elsevier; 2025 Accessed: Dec. 14, 2025. [Online]. https://www.sciencedirect.com/science/article/pii/S0026265X25037841
[8] Elsayed H, Wekalao J, Alqhtani HA, et al. Machine learning-enhanced terahertz plasmonic biosensor based on MXene-gold nanostructures for tuberculosis detection. In: Elsayed HA, Wekalao J, Alqhtani HA, Jumah M bin, Abukhadra MR, Bellucci S, Rajakannu A, editors. Sensing and Bio-Sensing Research. Elsevier; 2025 Accessed: Dec. 22, 2025. [Online]. https://www.sciencedirect.com/science/article/pii/S2214180425001187
[9] Ramya PR, Halder S, Gandhi S. Biosensing and imaging based on functionalized 2D nanomaterials. Wiley Online Library; 2025. p. 415–448. doi: 10.1002/9781394200375.CH18
[10] Murcia-Correa LS, Usuriaga-Najera OC, Berni LA, et al. Cathodic cage plasma deposition of Ag/Porous silicon as a scalable route to SERS substrates. Brazilian Journal of Physics. 2026;56. doi: 10.1007/S13538-025-01991-8
[11] Javed F, Shahid H, Hayat S, et al. Recent advances on macrocyclic compounds-based nano thin films for gas sensing applications. Vol. 23, Springer; 2026. doi: 10.1007/S13738-025-03288-8
[12] Solangi N, Kumar J, Premchand P, et al. MXene-based material for biosensing applications of emerging pollutants. Elsevier; 2026. Accessed: Jan. 3, 2026. [Online]. https://www.sciencedirect.com/science/chapter/edited-volume/pii/B9780443342707000195
[13] Wekalao J, Patel SK, Ben Khalifa S, et al. Optical-based aqueous solution detection by graphene metasurface surface plasmon resonance biosensor with behavior prediction using polynomial regression. Vol. 20, Springer; 2025. p. 2509–2530. doi: 10.1007/S11468-024-02464-5
[14] Aliqab K, Wekalao J, Alsharari M, et al. Designing a graphene metasurface organic material sensor for detection of organic compounds in wastewater, mdpi.com, 2023. Accessed: Jan. 3, 2026. [Online]. 10.3390/bios13080759
[15] Wekalao SK, Patel AKU, Armghan A, et al. Detection of proteins in a surface plasmon resonance biosensor based on hybrid metasurface architecture and behaviour prediction using random forest regression. Vol. 20, Springer; 2025. p. 5165–5185. doi: 10.1007/S11468-024-02712-8
[16] Alsaif H, Wekalao J, Ali NB, et al. Design and optimization of a MXene-based terahertz surface plasmon resonance sensor for malaria detection. Vol. 20, Springer; 2025. p. 2153–2163. doi: 10.1007/S11468-024-02455-6
[17] Ramola A, Shakya A, Balal N, et al. Investigation of Early Cancer Biomarker Sensing Using a PMMA–Gold Hybrid Quasi-D-Shaped Photonic-Crystal-Fiber-Based Surface Plasmon Resonance Biosensor, mdpi.com, 2026. Accessed: Jan. 3, 2026. [Online]. https://www.mdpi.com/2072-666X/17/1/68
[18] Juwel M, Utshob M, Al Mahmud A. Design and optimization of a hybrid SPR biosensor for highly sensitive detection of carcinoembryonic antigen. Elsevier; 2026. Accessed: Jan. 3, 2026. [Online]. doi: 10.1016/j.nxmate.2025.101526
[19] Sharma AK, Gupta BD. On the sensitivity and signal to noise ratio of a step-index fiber optic surface plasmon resonance sensor with bimetallic layers. In: Sharma AK, Gupta BD, editors. Opt Commu. Elsevier; 2005 Accessed: Jan. 3, 2026. [Online]. https://www.sciencedirect.com/science/article/pii/S0030401804010156
[20] Alsharari M, Wekalao J, Patel SK, et al. Enhanced sensing efficiency of ultra-narrow band graphene-based surface plasmon resonance refractive index sensor for biochemical applications and. Vol. 20, Springer; 2025. p. 1273–1284. doi: 10.1007/S11468-024-02372-8
[21] Patel SK, Wekalao J, Albargi HB, et al. Design and simulation of metasurface-enhanced graphene biosensors for cancer biomarker detection. Vol. 19, Springer; 2024. p. 3119–3130. doi: 10.1007/S11468-024-02224-5
[22] Wekalao J, Albargi HB, Patel SK, et al. Terahertz optical ultrasensitive glucose detection using graphene and silver surface plasmon resonance metasurfaces for biomedical applications. Vol. 20, Springer; 2025. pp. 373–385. doi: 10.1007/S11468-024-02278-5
[23] Wekalao J. Development of a high-sensitivity graphene-metal nanocomposite metasurfaces biosensor with machine learning integration for rapid detection of waterborne In: Wekalao J, editor. Plasmonics. Springer; 2025. 10.1007/S11468-024-02756-W
[24] Wekalao J, Baz A, Patel SK, et al. Numerical analysis of an advanced infrared-based graphene metasurface surface plasmon resonance sensor for COVID-19 detection. Diam Relat Mater. 2024;149(111601). doi: 10.1016/j.diamond.2024.11601

[25] Baz A, Wekalao J, Mandela N, et al. Design and performance evaluation of machine learning-based terahertz metasurface chemical sensor. IEEE Trans Nanobioscience. 2024;24(2):128–135. doi: 10.1109/TNB.2024.3453372
[26] Wekalao J, Mandela N, Langat W, et al. Enhanced fuel adulteration detection using surface plasmon resonance biosensor with machine learning optimization in the terahertz regime. Plasmonics. 2024;20:3355–3379. doi: 10.1007/s11468-024-02550-8
[27] Chen Z, Yang C, Fu H, et al. Surface plasmon resonance dual-channel H-shaped fiber sensor for simultaneous detection of refractive index and temperature. Springer; 2025. doi: 10.1007/S11468-025-03225-8
[28] Butt M A. Surface plasmon resonance-based biodetection systems: principles, progress and applications—A comprehensive review. Biosensors. 2025;15(1):35. doi: 10.3390/BIOS15010035
[29] Kohli K, Kedia J, & Gupta N, et al. Optical fibre sensors with LSPR sensing: A comprehensive review, pubs.aip.org, 2025. Accessed: Aug. 30, 2025. [Online]. https://pubs.aip.org/aip/acp/article-abstract/3227/1/060015/3339342
[30] Kushwaha A, Mishra A, Verma R, et al. Plasmonic sensor with BaTiO3 and si layers for dual application in environmental monitoring. Springer. 2025;20(9):7089–7100. doi: 10.1007/S11468-024-02750-2
[31] Ma X, Cheng H, Hou J, et al. Detection of breast cancer based on novel porous silicon bragg reflector surface-enhanced Raman spectroscopy-active structure. In: Ma X, Cheng H, Hou J, Jia Z, Wu G, Lü X, Li H, Zheng X, Chen C, editors. ChOpL. Vol. 18, opg.optica.org; 2020. p. 051701. doi: 10.3788/COL202018.051701
[32] Li L, Zhong M, Wu Z, et al. Nanozyme-enhanced tyramine signal amplification probe for preamplification-free myocarditis-related miRNAs detection In: Li L, Li J, Zhong M, Wu Z, Wan S, Li X, Zhang Y, Lv K, editors. Chem Eng J. Vol. 503, Elsevier; 2025. p. 158093. doi: 10.1016/J.CEJ.2024.158093
[33] He Q, Luo H, Chen L, et al. Nanographite-based fluorescent biosensor for detecting microRNA using duplex-specific nuclease-assisted recycling. In: He Q, Luo H, Chen L, Domg J, Chen K, Ning Y, editors. Luminescence. Vol. 35, Wiley Online Library; 2020. p. 347–354. doi: 10.1002/BIO.3733
[34] Tang Y, Li Y, Chen P, et al. Nucleic acid aptamer-based sensors for bacteria detection: A review. In: Tang T, Li Y, Chen P, Zhong S, Yang Y, editors. Bioessays. Vol. 47, Wiley Online Library; 2025. doi: 10.1002/BIES.202400111
[35] Yi J, Xiao W, Li G, et al. The research of aptamer biosensor technologies for detection of microorganism. In: Yi J, Xiao W, Li G, Wu P, He Y, Chen C, He Y, Ding P, Kai T, editors. Appl Microbiol Biotechnol. Vol. 104, Springer; 2020. p. 9877–9890. doi: 10.1007/S00253-020-10940-1
[36] Li D, Yin J, Yu Z, et al. Artificial intelligence-assisted colorimetric sensor array based on supramolecular self-assembled nanozymes for visual monitoring of pesticide residues. Sensors and Actuators B: Chemical. 2025; 444. doi: 10.1016/J.SNB.2025.138493
[37] Du B, Tian X, Chen Z, et al. Ultrasensitive optoelectronic biosensor arrays based on twisted bilayer graphene superlattice. In: Du B, Tian T, Chen Z, Ge Y, Chen C, Gao H, Liu Z, Tung J, Fixler D, Wei S, Chen S, Zhang H, editors. Natl Sci Rev. Vol. 12, academic.oup.com; 2025. doi: 10.1093/NSR/NWAF357
[38] Chen Z, Li J, Fan T, et al. A CRISPR/Cas12a-empowered surface plasmon resonance platform for rapid and specific diagnosis of the omicron variant of SARS-CoV-2 In: Chen Z, Li J, Li T, Fan T, Meng C, Li C, Kang J, Chai L, Hao Y, Tang Y, Al-Hartomy OA, editors. Natl Sci Rev. Vol. 9, academic.oup.com; 2022. doi:10.1093/NSR/NWAC104
[39] Chen Z, Li J, Fan T, et al. A CRISPR/Cas12a-empowered surface plasmon resonance platform for rapid and specific diagnosis of the omicron variant of SARS-CoV-2. Natl Sci Rev. 2022;9(8):1–10. doi: 10.1093/NSR/NWAC104
[40] Du B, Tian X, Chen Z, et al. Ultrasensitive optoelectronic biosensor arrays based on twisted bilayer graphene superlattice. Natl Sci Rev. 2025;12(10):1–10. doi: 10.1093/NSR/NWAF357
[41] Li D, Yin J, Yu Z, et al. Artificial intelligence-assisted colorimetric sensor array based on supramolecular self-assembled nanozymes for visual monitoring of pesticide residues. Sens Actuators B Chem. 2025;444:138493. doi: 10.1016/J.SNB.2025.138493
[42] He Y, Bao M, Chen Y, et al. Accuracy characterization of Shack–Hartmann sensor with residual error removal in spherical wavefront calibration. In: He M, Bao M, Chen Y, Ye H, Fan J, Shi G, editors. Light: Advanced Manufacturing. Vol. 4. light-am.com; 2024. p. 2–11. doi: 10.1109/TNB.2022.3159532
[43] Singh MK, Pal S, Prajapati YK. Design and analysis of an SPR sensor based on antimonene and platinum for the detection of formalin. In: Singh MK, Pal S, Prajapati YK, editors. IEEE Transactions on Nano Bioscience. Vol. 22, 2023. p. 106–112. doi: 10.1109/TNB.2022.3159532
[44] Kumar R, Pal S, Prajapati Y, et al. Sensitivity improvement of a MXene-immobilized SPR sensor with ga-doped-zno for biomolecules detection. In: Kumar R, Pal S, Prajapati YK, Kumar S, Saini JP, editors. IEEE Sens J; 2022. ieeexplore.ieee.org. Accessed: Jan. 3, 2026. [Online]. https://ieeexplore.ieee.org/abstract/document/9721092/
[45] Tiwari H, Dwivedi Y, & Singh R, et al. Deep learning-enabled de-noising of fiber Bragg grating-based glucose sensor: Improving sensing accuracy of experimental data" mdpi.com, 2024. Accessed: Jan. 3, 2026. [Online]. doi: 10.3390/photonics11111058
[46] Rana J, Sharma AK, Prajapati YK, et al. Intervention of machine learning and explainable artificial intelligence in fiber optic sensor device data for systematic and comprehensive performance-optimization. In: Rana J, Sharma AK, Prajapati YK, editors. IEEE Sens Lett. Vol. 8 2024. doi: 10.1109/LSENS.2024.3445324

[47] Srivastava R, Kumar V, Tyagi S, et al. On the feasibility of particle swarm optimization method for inverse design of high-performance SPR biosensor. In: Srivastava R, Kumar V, Tyagi S, Pal S, Sharma AK, Prajapati YK, editors. IEEE Sens J. Vol. 24, 2024. p. 16242–16249. doi: 10.1109/JSEN.2024.3381250
[48] Tiwari H, Dwivedi YS, Singh R, et al. Exploring deep learning models aimed at favorable optimization and enhancement of fiber optic sensor's performance. In: Tiwari H, Dwivedi YS, Singh R, Kaur B, Prajapati YK, Krishna R, Singha NS, Sharma AK, editors. IEEE Sens J. Vol. 23, ieeexplore.ieee.org; 2023. p. 20330–20337. doi: 10.1109/JSEN.2023.3296199
[49] Cotoraci C, Ciceu A, Sasu A, et al. Natural antioxidants in Anemia treatment 2021. doi: 10.3390/ijms22041883
[50] Hess SY, Owais A, Jefferds MED, et al. Accelerating action to reduce anemia: Review of causes and risk factors and related data needs 2023. doi: 10.1111/nyas.14985
[51] Garcia-Casal MN, Dary O, Jefferds ME, et al. Diagnosing anemia: challenges selecting methods, addressing underlying causes, and implementing actions at the public health level. Ann N Y Acad Sci. 2023;1524(1):37–50. doi: 10.1111/nyas.14996
[52] Stanley AY, Wallace JB, Hernandez AM, et al. Anemia in pregnancy: screening and clinical management strategies. MCN The American Journal of Maternal/Child Nursing. 2022;47(1):25–32. doi: 10.1097/NMC.0000000000000787
[53] Gumaih HS, Mollah MA, Adam YS, et al. Prism based surface plasmon resonance sensor using Ag/BaTiO3/BP layers for cancer detection. Plasmonics. 2024;20:3997–4006. doi: 10.1007/s11468-024-02600-1
[54] Mudgal N, Saharia A, Agarwal A, et al. Modeling of highly sensitive surface plasmon resonance (SPR) sensor for urine glucose detection. Opt Quantum Electron. 2020;52(6):307. doi: 10.1007/S11082-020-02427-0
[55] Rafi SA, Emon W, Rafsan AA, et al. Optical based surface plasmon resonance sensor for the detection of the various kind of cancerous cell. Cell Biochem Biophys. 2024;83:689–715. doi: 10.1007/s12013-024-01503-6
[56] Kumar R, Sharma Y, T. S, et al. Detection of urine glucose concentration using zirconium nitride surface plasmon resonance sensor. Plasmonics. 2025;20(8):5757–5766. doi: 10.1007/S11468-025-02853-4
[57] Shivangani, Sahu A, Kumar D, et al. Design and analysis of surface plasmon resonance sensor utilizing silver, nickel, and black phosphorous for various cancer detection. Plasmonics. 2025;20(8):6623–6639. doi: 10.1007/S11468-025-02961-1
[58] Karki B, Pal A, Uniyal A, et al. Design and optimization of a novel SPR sensor for detecting cancerous cells: a simulation-based study. Plasmonics. 2025;20(8):6027–6035. doi: 10.1007/S11468-025-03057-6